Published in final edited form as:

Nat Cancer. 2021 December ; 1(12): 1188–1203. doi:10.1038/s43018-020-00139-8.

Mutations in *BRCA1* and *BRCA2* differentially affect the tumor microenvironment and response to checkpoint blockade immunotherapy

Robert M. Samstein[1,2,3,12], **Chirag Krishna**[4,12], **Xiaoxiao Ma**[5,12], **Xin Pei**[1], **Ken-Wing Lee**[5], **Vladimir Makarov**[6], **Fengshen Kuo**[6], **Jonathan Chung**[3], **Raghvendra M. Srivastava**[6], **Tanaya A. Purohit**[6], **Douglas R Hoen**[6], **Rajarsi Mandal**[5], **Jeremy Setton**[1], **Wei Wu**[5], **Rachna Shah**[1], **Besnik Qeriqi**[7], **Qing Chang**[7], **Sviatoslav Kendall**[6], **Lior Braunstein**[1], **Britta Weigelt**[8], **Pedro Blecua Carrillo Albornoz**[1,9], **Luc G.T. Morris**[5,6,10], **Diana L Mandelker**[8], **Jorge S. Reis-Filho**[8], **Elisa de Stanchina**[7], **Simon N. Powell**[1], **Timothy A. Chan**[1,5,6,11,*], **Nadeem Riaz**[1,5,6,*]

[1]Dept. of Radiation Oncology, Memorial Sloan Kettering Cancer Center, New York, NY 10065

[2]Dept. of Radiation Oncology, Mount Sinai Hospital, New York, NY 10029

[3]Precision Immunology Institute at Icahn School of Medicine at Mount Sinai, New York, NY 10029

[4]Computational and Systems Biology Program, Memorial Sloan Kettering Cancer Center, New York, NY 10065

[5]Human Oncology and Pathogenesis Program, Memorial Sloan Kettering Cancer Center, New York, NY 10065

[6]Immunogenomics and Precision Oncology Platform, Memorial Sloan Kettering Cancer Center, New York, NY 10065

[7]Antitumor Assessment Core Facility, Memorial Sloan Kettering Cancer Center, New York, NY 10065

[8]Dept. of Pathology, Memorial Sloan Kettering Cancer Center, New York, NY 10065

[9]Cancer and Leukemia Epigenetics and Biology Program, Josep Carreras Leukaemia Research Institute, Barcelona, Spain

[10]Dept. of Surgery, Memorial Sloan Kettering Cancer Center, New York, NY 10065

[11]Center for Immunotherapy and Precision Immuno-Oncology, Dept. of Radiation Oncology, Cleveland Clinic, OH 44195

[12]These authors contributed equally: Robert M. Samstein, Chirag Krishna, Xiaoxiao Ma

Abstract

---

[*]Correspondence to: chant@mskcc.org (T.A.C), riazn@mskcc.org (N.R.).

AUTHOR CONTRIBUTIONS

RMS, CK, XM, TAC and NR wrote the manuscript with constructive feedback from all the authors. RMS, CK, VM, FK, SK, XP, PBCA and DH performed computational analyses. RMS, XM, KWL, RM, JS, EdS, SNP, TAC and NR were involved in experimental design. RMS, KWL, XM, JC, WW, RMS, TAP, RS, BQ and QC performed experiments. RMS, CK, TAC, NR, SNP, JSR, LB, LGTM and DLM were involved in data interpretation and manuscript preparation.

Immune checkpoint blockade (ICB) has improved outcomes for patients with advanced cancer, but the determinants of response remain poorly understood. Here we report differential effects of mutations in the homologous recombination genes BRCA1 and BRCA2 on response to ICB in mouse and human tumors, and further show that truncating mutations in BRCA2 are associated with superior response compared to those in BRCA1. Mutations in BRCA1 and BRCA2 result in distinct mutational landscapes and differentially modulate the tumor-immune microenvironment, with gene expression programs related to both adaptive and innate immunity enriched in BRCA2-deficient tumors. Single-cell RNA sequencing further revealed distinct T cell, natural killer, macrophage, and dendritic cell populations enriched in BRCA2-deficient tumors. Taken together, our findings reveal the divergent effects of BRCA1 and BRCA2-deficiency on ICB outcome, and have significant implications for elucidating the genetic and microenvironmental determinants of response to immunotherapy.

Introduction

The initial success of immune checkpoint blockade (ICB) for the treatment of cancer patients has invigorated interest in harnessing the anti-tumor potential of the immune system across many cancer types. However, durable responses to ICB are limited to a minority of patients. Our group and others have demonstrated that tumor cell-intrinsic characteristics such as high tumor mutational burden (TMB)—a proxy for increased presentation of immunogenic neoantigens—are associated with improved response to immunotherapy. [1–4] It should be noted, however, that high TMB alone does not always predict ICB response.

Recent studies have suggested that alterations in the DNA damage response (DDR) pathway may influence response to ICB. [3,5] Notably, mismatch repair (MMR) deficiency, which results in microsatellite instability (MSI) and elevated mutational load, is an FDA-approved biomarker for the clinical use of anti-PD1 therapy. [6] The homologous recombination (HR) pathway is the next most commonly altered DDR pathway in cancer, [7] often due to genetic alterations affecting the core genes *BRCA1* or *BRCA2*. The HR pathway can be altered by somatic or germline mutations, [8] which predispose to different cancer types depending on the mutation. For example, germline mutations in *BRCA1* are associated with estrogen receptor (ER)-negative breast and ovarian cancers, whereas those in *BRCA2* are associated with ER-positive breast, ovarian, prostate and pancreatic cancers.

Recent reports have suggested that mutations in DDR and HR pathways may influence response to ICB. [1,9,10] In addition, there is burgeoning evidence suggesting that HR-deficient cancers—in particular, breast and ovarian cancers—are characterized by heterogeneous immune landscapes. [11,12] However, rates of patient response to ICB in HR-associated cancer types (breast, prostate, pancreatic, and ovarian) remain low, [13,14] likely stemming from an incomplete understanding of the genetic and microenvironmental determinants of response to ICB in the setting of HR deficiency. Here we sought to explore the impact of HR deficiency on the immune microenvironment and outcome after ICB treatment in murine and human tumors.

RESULTS

Pan-cancer pathway analysis demonstrates an association of homologous recombination deficiency with improved response to immune checkpoint inhibitors

Using a pan cancer dataset of patients treated with ICB, [15,16] we examined the effect of somatic truncating mutations in genes from KEGG pathways on patient overall survival (OS) after ICB administration (Fig. 1a). Truncating mutations in DNA repair pathways such as nucleotide excision repair, mismatch repair and base excision repair were associated with improved OS after ICB. Notably, mutations in genes of the HR pathway were associated with improved OS (hazard ratio 0.55, $p = 0.005$, $FDR < 0.10$).

Syngeneic murine models of Brca2 deficiency demonstrate improved response to immune checkpoint inhibitors

Given the association between HR genes and response to ICB and the fact that *BRCA1* and *BRCA2* are the two most recurrently mutated genes in this pathway, we sought to test the functional impact of truncating mutations affecting these genes on the immune microenvironment through multimodal genomic analyses of murine and human tumors (Fig. 1b). We first focused on the impact of mutations in *BRCA2*, due to its core function in HR repair and less pleiotropic role in other pathways. [1718] We used CRISPR-Cas9-nickase genome editing to generate a murine orthotopic 4T1 breast cancer cell line with BRCA2 deficiency (Extended Data Fig 1). Using this isogenic murine model system, we observed that Brca2^{null} cells were deficient in their ability to recruit Rad51 to sites of double strand breaks after irradiation, and markedly more sensitive to the PARP inhibitor olaparib *in vitro* compared to the parental cell line (Fig. 2a–c). Karyotype analysis of Brca2^{null} cells revealed evidence of increased chromatid breaks and exchanges consistent with genomic instability (Fig. 2d and Extended Data Fig 2d). Taken together, these findings are consistent with a loss of competent HR DNA repair in the 4T1 Brca2^{null} cells. A similar approach was taken in a second isogenic syngeneic system, the CT26 colorectal cancer model, to induce BRCA2 deficiency (Extended Data Fig. 2a–c,e–f). Whole-genome sequencing (WGS) of the 4T1 parental and Brca2^{null} cells after passaging for 4 months revealed an accumulation of SNVs and indels consistent with prior analyses of BRCA2-mutant human cancers (Fig. 2e). Analysis of the mutational signature from these samples, after subtracting background mutagenesis from parental cell lines, [19] demonstrated modest cosine similarity to previously described mutational signatures associated with HRD, namely Signature 3 (Extended Data Fig 3a–b). Importantly, deletions in the Brca2^{null} model were longer than 1bp and enriched for microhomology at the breakpoints (Fig 2f & Extended Data Fig 3c), both cardinal features of HRD.[20,21]

We next evaluated the immunologic consequences of BRCA2 deficiency using this isogenic system. Flow cytometric analysis of tumor infiltrating lymphocytes in 4T1 mammary fat pad tumors demonstrated increased proportions of CD4 and CD8 T cells (Fig. 2g). We subsequently performed bulk RNA-sequencing (RNA-seq) from *in-vivo* tumors to further delineate the immune differences between 4T1 Brca2^{null} and 4T1 Brca2^{WT} tumors. Differential expression analysis of 4T1 Brca2^{null} and 4T1 Brca2^{WT} tumors yielded 4,637 significantly differentially expressed genes at $FDR < 0.05$ (Extended Data Fig. 4a and

Supplementary Table 1). An unbiased pathway analysis based on the differentially expressed genes between 4T1 Brca2^{null} and 4T1 Brca2^{WT} tumors yielded processes related to T cell activation and cell-cell adhesion, as well as several significant terms related to innate immune and antiviral responses (Extended Data Fig. 4b). To further interrogate whether these pathways were particularly enriched in 4T1 Brca2^{null} and 4T1 Brca2^{WT} tumors, we performed gene set enrichment analysis (GSEA) of 4T1 Brca2^{null} and 4T1 Brca2^{WT} tumors using known signatures curated from MSigDb (Supplementary Table 1). Terms related to immune response and T cell activation were strongly enriched in 4T1 Brca2^{null} compared to Brca2^{WT} tumors (Extended Data Fig 4c–d). Extending our earlier pathway analysis, we observed several terms related to cytokine signaling, IFNA signaling and Natural Killer cell (NK)-mediated cytotoxicity enriched in Brca2^{null} compared to Brca2^{WT} tumors (Extended Data Fig. 4f–g). Curiously, terms related to epithelial to mesenchymal transition (EMT) and angiogenesis were also enriched in this differential analysis (Extended Data Fig. 4b). Taken together with the other pathways enriched in our differential expression analyses, these data may suggest immunological consequences of EMT in Brca2^{null} tumors, such as tumor associated macrophage activity, or even NK-mediated cytotoxicity as suggested by others.[22,23]

Subsequently, we sought to investigate whether Brca2 deficiency would affect response to immune checkpoint inhibitor therapy in this isogenic system. While parental mammary fat pad tumors showed only limited response, 4T1 Brca2 deficient tumors exhibited significant growth delay in response to anti-PD1 or combination anti-Pd1/anti-Ctla4 immune checkpoint blockade treatment (Fig. 2h). A similar difference in response to anti-Pd1 therapy was observed between Brca2^{null} tumors and a parental line in a CT26 colorectal murine model (Fig. 2i). Further, similar results were obtained with additional 4T1 Brca2^{null} and CT26 Brca2^{null} clones (Extended Data Fig 2g–h). Increased T cell infiltration was observed by immunofluorescence in 4T1 Brca2^{null} tumors at baseline or after immune checkpoint blockade (Figs. 2j and 2k). Taken together, these data demonstrate that in isogenic murine models, Brca2 deficiency results in an inflamed tumor microenvironment with improved response to ICB.

Mutations in *Brca1* and *Brca2* mediate distinct mutational landscapes and effects on the immune microenvironment in isogenic murine tumors

We next sought to determine if mutations in *BRCA1* caused a similar effect on the tumor microenvironment and response to ICB as mutations in *BRCA2*. In the context of breast cancers, *BRCA1* germline mutations have been shown to be associated with a more conspicuous inflammatory infiltrate than sporadic and BRCA2-deficient breast cancers, and have been assumed to be one of the likeliest subsets of breast cancers to respond to ICB.[24,25] To investigate the role of BRCA1 deficiency in an isogenic setting, we generated 4T1 *Brca1*^{null} cell lines using CRISPR-Cas9-nickase targeting. 4T1 Brca1^{null} cells demonstrated sensitivity to PARP inhibition (Fig. 3a,b). WGS of Brca1^{null} cells revealed an accumulation of SNVs, but a more modest increase in indels compared to Brca2^{null} cells (Fig 3c). Furthermore, the mutational signature of Brca1^{null} cells also demonstrated similarity to signature 3, similar to Brca2^{null} cells (Extended Data Fig 3d). Interestingly, although deletion length and microhomology were increased in Brca1^{null} cells compared to parental cells, these differences were more modest compared to Brca2^{null} cells (Fig 3d and Extended Data Fig. 3e). Contrary to our expectations, 4T1 Brca1^{null} tumors did not demonstrate an increased response to Pd-1 or combination Pd-1/Ctla4 blockade, consistent with a previous report on a Brca1^{null} murine model and response to ICB (Fig. 3e). [26]

Given the strikingly different responses to checkpoint blockade immunotherapy observed between our BRCA1 and BRCA2-deficient murine tumor models, we hypothesized that deficiency in BRCA1 and BRCA2 may be associated with distinct tumor-immune microenvironments. To explore the consequences of *BRCA1* and *BRCA2* mutations on the immune microenvironment, we performed comparative RNA-seq analyses of 4T1 Brca1^{null} and Brca2^{null} tumors. Immune deconvolution analysis revealed significant separation between BRCA1- and BRCA2- deficient murine tumors (Fig. 3f, Permanova P = 0.01). Differential expression analysis yielded 6,881 differentially expressed genes at FDR $p < 0.05$ (Extended Data Fig. 5a) and unsupervised pathway analysis of these genes identified multiple terms related to T-cell cytotoxicity and antiviral responses enriched in Brca2^{null} tumors relative to Brca1^{null} tumors (Extended Data Fig. 5b). GSEA revealed terms related to TCR signaling and cytotoxic Th1 responses (Fig 3g–h and Supplementary Table 2). Moreover, direct examination of significantly differentially expressed genes between Brca2^{null} and Brca1^{null} tumors yielded programs related to interferon gamma signaling, T cell activation and antigen presentation (Extended Data Fig. 5c–e) upregulated in Brca2^{null} tumors, suggesting that Brca2 deficiency may drive both adaptive and innate immune activation. Furthermore, GSEA yielded pathways related to innate immune activity were enriched in Brca2^{null} tumors (Extended Data Fig. 5f–h and Supplementary Table 2). Furthermore, comparative analysis of RNA-seq from Brca2^{null} and Brca1^{null} tumors after treatment with anti-Pd1 demonstrated similar programs upregulated in Brca2^{null} tumors (Extended Data Fig. 6).

We next sought to isolate tumor intrinsic effects of *Brca1* and *Brca2* alterations, and thus conducted differential gene expression analysis between 4T1 Brca1^{null} and Brca2^{null} cell lines in in vitro culture system. We noted differential expression of several genes associated with regulatory, checkpoint or immunosuppressive activity in Brca1^{null} cell lines compared to Brca2^{null} cell line, including *Arg1, Braf, Cd276, Cxcl5, Hmgb1, Tgfb2, Tgfbr1 and Tgfbr2* at FDR < 0.05 (Extended Data Fig. 5i and Supplementary Table 3). Brca2^{null} cell line upregulated factors previously associated with innate immune cell activation including *Adora1*, *Il33* and *Wnt5a.* [27–29] (Extended Data Fig. 5i). These differences, coupled with our murine data suggesting increased immune activation due to BRCA2 deficiency, led us to hypothesize that Brca1 deficiency may result in up-regulation of genes with immunoregulatory or suppressive activity. To evaluate this hypothesis, we constructed a gene set from the literature comprised of immunoregulatory and immunosuppressive genes (Supplementary Table 4). [30–34] We evaluated differential enrichment of the gene set between Brca1^{null} Brca2^{null} cell lines in culture using GSEA. This analysis revealed enrichment in Brca1^{null} cells when compared to Brca2^{null} cells (Fig. 3i and Supplementary Table 3). Genes in the leading edge of the analysis driving enrichment of the gene set in Brca1^{null} cells included multiple immunoregulatory genes such as Ido1, *Vtcn1, Cxcl5, Pdgfc, Vsir, Pdcd1*, and *Entpd1* (Supplementary Table 3). These data suggest that tumor-cell intrinsic up-regulation of genes associated with immunosuppression may occur in BRCA1-deficient cancers, as previously suggested by others.[34–36] Altogether, these data suggest that in an isogenic setting, mutations in *Brca1* and *Brca2* lead to distinct immune microenvironments.

Distinct tumor-immune microenvironments in BRCA1 and BRCA2- deficient tumors from TCGA

To define the differences in the tumor-immune microenvironment between BRCA1- and BRCA2-deficient tumors observed in our murine data, we analyzed RNA-seq data from patients with pathogenic biallelic mutations in *BRCA1* or *BRCA2* in the Cancer Genome Atlas (TCGA) breast cancer dataset [37] We first performed single sample GSEA (ssGSEA) using gene sets for well-characterized immune populations followed by an exploratory principle component analysis, which demonstrated that tumors with germline or somatic biallelic *BRCA1* or *BRCA2* pathogenic mutations formed two distinct clusters, particularly with respect to innate immune populations (Fig. 4a and Extended Data Fig. 7a–b).

We next performed GSEA analyses using the immunoregulatory gene set evaluated in our murine data. To control for previously published immunological differences between estrogen receptor (ER)+/− tumors, BRCA1 and BRCA2-deficient tumors were compared to each other (Fig. 4b and Supplementary Table 5) and to their non-mutated histological counterparts (Figs. 4c and 4d). BRCA1-deficient triple-negative tumors (TNBCs, i.e. lacking ER, progesterone receptor and HER2 expression) were enriched in the immunoregulatory gene set when compared to BRCA1-proficient TNBCs (Supplementary Table 5), whereas this was not the case for BRCA2-deficient tumors and their histologic controls (Supplementary Table 5), suggesting a BRCA1-specific immunoregulatory effect. This difference in enrichment of the immunoregulatory gene set between BRCA1-deficient and BRCA2-deficient tumors was validated in the METABRIC dataset (Fig. 4e and Supplementary Table 5).[38] Genes in the leading edge of the GSEA that overlapped between the TCGA and METABRIC datasets included several regulatory and checkpoint molecules such as *CD47, CTLA4, CXCL5, ICOS, IDO1, LAG3, PDCD1LG2, SIRPA, TNFRSF9* (4–1BB) and *VEGFA* (Supplementary Table 5). These results suggest that the tumor-immune microenvironmental differences between BRCA1 and BRCA2-deficient tumors may be partially driven by tumor-cell intrinsic consequences of BRCA1 loss.

Interestingly, BRCA1- and BRCA2-deficient breast tumors were recently associated with distinct patterns of genomic alterations including increased single nucleotide variants (SNVs) and insertions or deletions (indels) with microhomology in BRCA2 deficient tumors, whereas BRCA1 deficient tumors had elevated levels of large rearrangements and tandem duplications.[20,39,40] Indeed, we found that BRCA2 deficient ER+ tumors had higher numbers of SNVs and indels, and thus, predicted neopeptide counts indicative of heightened potential immunogenicity, whereas levels of these alterations in BRCA1-deficient TNBCs were not significantly different from *BRCA1/BRCA2* wild-type TNBCs (Extended Data Fig. 7c–e). Evaluation of single-nucleotide substitutions demonstrated BRCA2 deficient tumors were more distinct from their histologic controls than BRCA1 deficient tumors, although differences in signature 3 were minimal between the two (Extended Data Fig. 7f–h). BRCA2 deficient tumors also had a more pronounced difference in the distribution of indel lengths compared to histologic controls than BRCA1 deficient tumors (Extended Data

Fig. 7i). These results mirror findings from isogenic Brca1 and Brca2 deficient murine tumor models, and together suggest that differences in the mutational landscape between *BRCA1* and *BRCA2* may partly contribute to differences in immunogenicity. Furthermore, relative to BRCA2-deficient tumors, BRCA1-deficient tumors were associated with increased levels of copy number alterations across the genome (Extended Data Fig. 7j–l), which have been linked to worse response to immunotherapy. [41,42] These results suggest that in human tumors, mutations in *BRCA1* and *BRCA2* differentially modulate the tumor-immune microenvironment which may be partially due to distinct mutational and copy-number profiles.

Differential response to ICB in patients with BRCA2 deficiency compared to *BRCA1* mutations

Given the improved response to ICB observed in our Brca2^{null} murine tumors compared to our Brca1^{null} models and the distinct tumor-immune microenvironments observed between BRCA1-deficient and BRCA2-deficient murine and *BRCA1*- and *BRCA2*-associated human tumors, we hypothesized that patients with pathogenic mutations in *BRCA1* and *BRCA2* would respond differently to ICB. Accordingly, in an exploratory retrospective analysis, we analyzed a pan-cancer cohort of patients profiled with the FDA-approved MSK-IMPACT targeted capture sequencing assay with identifiable somatic or germline truncating mutations in *BRCA2.* [15,16] Following manual curation and review of radiographic responses of identifiable patients, we noted a 44.4% rate of clinical benefit among patients receiving ICB with truncating *BRCA2* germline or somatic mutations across multiple cancer types (n=18, Figure 4f). As many patients receiving MSK-IMPACT did not have consent for germline testing, we received IRB approval to call germline variants and perform an anonymized analysis of overall survival after ICB. On univariable cox regression analysis, we found that truncating germline or somatic mutations in *BRCA2* were associated with improved overall survival after ICB (N = 67; Hazard ratio 0.48, 95% CI 0.29–0.80, P = 0.004) relative to truncating mutations in *BRCA1* (N = 28; Hazard ratio 0.76, 95% CI 0.48–1.54, P = 0.45) (Fig. 4g). Moreover, on multivariable analysis, the effect of *BRCA2* mutations on improved overall survival after ICB also remained significant after controlling for other clinical covariates (HR 0.50, 95% CI 0.30–0.83, P = 0.008) (Fig. 4h). Thus, pathogenic mutations in *BRCA1* and *BRCA2* differentially modulate the tumor-immune microenvironment and response to ICB, though prospective validation of these findings will be required before they can be utilized in a clinical setting.

Single cell sequencing reveals enrichment of distinct lymphoid and myeloid subpopulations in BRCA2 and BRCA1-deficient tumors

To further explore the mechanisms driving improved response to ICB in BRCA2-deficient tumors and resistance with BRCA1-deficiency, we next sought to study the specific immune cell types that differ between Brca2^{null} and Brca1^{null} murine tumors. Thus, we performed single cell RNA-sequencing of all CD45+ cells sorted from ICB-untreated 4T1 Brca1^{null}, Brca2^{null}, and WT tumors. 53136 cells passed quality control (Methods and Extended Data Fig. 8a–c), of which 10963, 19691, and 22482 cells were derived from Brca1^{null}, Brca2^{null}, and WT murine tumors, respectively. Dimensionality reduction followed by Phenograph clustering yielded 25 distinct clusters (Fig. 5a), [43]indicating marked heterogeneity within the immune compartment comprised of various lymphoid and myeloid populations (Fig. 5b) and consistent with recent reports. [11]

We next sought to phenotype the specific T cell clusters within the microenvironment of Brca1^{null}, Brca2^{null}, and WT tumors. Analysis of previous established marker genes yielded significant heterogeneity in T cell state, with distinct cytotoxic, memory and exhausted populations infiltrating the microenvironment (Fig. 5c–d). Clusters 0 (C0) and C9 were the two principal *Cd8a+* T cell clusters, with C0 demonstrating hallmarks of naïve T cells, i.e. expression of Tcf7 and Sell. Curiously, this cluster also demonstrated markers typical of an alternatively activated or innate-like phenotype, characterized by high expression of the cytotoxic markers *Nkg7* and *Ly6c1/2*. C9 resembled conventional *Cd8a+* exhausted T cells, demonstrating high expression of Pdcd1, Lag3, and Tnfrsf18. C12 displayed scattered expression of both *Cd8a* and *Cd4*, and also expressed markers of activation and proliferation, i.e. *Mki67*, *Top2a*, and *Birc5*. Similar to *Cd8a*+ T cells, we also detected heterogeneity within the *Cd4*+ T cell compartment. The *Cd4*+ T cell clusters C1, 3, and 5 demonstrated similar transcriptional profiles, with subtle differences in marker gene expression. For example, C1 was distinguished by high expression of arginosuccinate synthase (Ass1), previously implicated in overcoming arginase induced immunosuppression by *Cd4+* T cells. [44] C4, another *Cd4+* T cell cluster, expressed markers of interferon signaling such as *Stat1* and *Ifit1/3* while C5 is composed by *Cd4*+ T cells expressing high levels of *Lef1* and *Tcf7*, previously characterized as genes defining T cell states associated with response to ICB in melanoma. [45] Finally, C6 expressed markers of activation and memory such as *Klf6*, *Gzmb*, and *Cd44*, and scattered expression of *Pdcd1*.

We next asked whether particular subpopulations were differentially enriched in Brca2^{null} or Brca1^{null} tumors. Indeed, we observed significant differences in cluster proportions between Brca1^{null}, Brca2^{null} and parental tumors (Fig. 5e and Extended Data Fig 8d). Critically, we observed enrichment of the conventionally activated/exhausted *Cd8a+ Pdcd1+* cluster C9, as well as *Cd4*+ clusters C5 and C6, in Brca2^{null} cells relative to Brca1^{null}cells (Fig. 5e). Notably, we noted significant enrichment of NK cells (C24) in Brca2^{null} tumors relative to Brca1^{null} tumors (Fig. 5e). These data suggest that Brca1 and Brca2 loss differentially affect the lymphoid compartment of the tumor-immune microenvironment, and reveal that both *Cd4+* and *Cd8a*+ subsets, along with NK cells, may differ in proportion between Brca1^{null} and Brca2^{null} tumors. Importantly, the prevalence of cytotoxic and exhausted *Cd4+* and *Cd8a+* populations in Brca2^{null} tumors may suggest that these cell types may also underlie differential responses to ICB. Moreover, these results are consistent with and extend those observed in our bulk RNA-seq analyses, in which terms related to *Cd8a+* and *Cd4+* T cell activation, as well as innate immunity were also observed.

Given the enrichment of innate immune genes revealed by bulk RNA-seq analysis coupled with increased NK infiltration in Brca2^{null} tumors observed in single cell analysis of lymphoid populations, we next sought to assess the diversity of myeloid populations in Brca1^{null} and Brca2^{null} tumors. Re-clustering of all *Cd3-/Cd14+* populations yielded 11 clusters (Fig. 6a), composed of predominantly of tumor-associated macrophage (TAM) and dendritic cell populations. Broadly, TAMs within the breast microenvironment expressed combinations of pro-inflammatory and suppressive markers such as *Arg1, Nos2, Vegfa,* *Apoe*, and *Trem2* (Fig. 6c–d). In addition, some TAM populations were characterized by high expression of interferon signaling genes, such as *Ifitm1/3*, and *Isg15*.

Recent reports have described extensive macrophage infiltration in breast tumors, [46] and others have described remodeling of the myeloid compartment after ICB. [47] Consistent with and extending these data, we found that TAMs were differentially enriched in Brca1^{null} and Brca2^{null} tumors, such as TAM C3 enriched in Brca2^{null} tumors relative to Brca1^{null} tumors, which displayed high expression of pro-inflammatory signaling markers *Isg15* and *Tlr4*, as well as *Ccl3* (Fig. 6d–e). A similar effect was observed for C6, which expressed the pro-inflammatory markers *Il12a* and *Ccr9* (Fig. 6d–e) and was enriched in *Brca2^{null}* cells. Interestingly, we also observed enrichment of plasmacytoid dendritic cell populations (C8) in Brca2^{null} cells relative to Brca1^{null} cells (Fig. 6e and Extended Data Fig. 8b). In contrast, several TAM populations (e.g. C4) expressing immunosuppressive markers such as *Pdl1, Vegfa, Anxa1 and Mmp8*, as well as the pro-inflammatory marker *Nos2*, were enriched in *Brca1^{null}* cells (Fig. 6e). Further, flow cytometry analysis demonstrated enrichment of cytotoxic T cell populations and dendritic cells in Brca2^{null} tumors relative to Brca1^{null} tumors (Extended Data Fig. 9a–b), and immunosuppressive TAM populations in Brca1^{null} tumors relative to Brca2^{null} tumors (Extended Data Fig. 9a–b).

Finally, we sought to clarify the cellular states differentially enriched in these Brca1 and Brca2-deficient tumors after ICB administration (Fig 7a–b, Extended Data Fig 10a–d). We first examined the enrichment of multiple T cell populations in Brca2^{null} tumors treated with Pd-1/Ctla4 blockade (Extended Data Fig 10d). Two of these clusters were *Cd8a+*, with one expressing high levels of *Tcf7* and *Lef1* (Fig 7a,c), previously reported to be important for ICB response. [45] Importantly, the other T cell cluster expressed high levels of the cytotoxic markers *Gzmb/k*, as well as *Pdcd1* (Fig 7a,c). Consistent with our untreated analysis, we found a *Cd4+* cluster expressing high levels of *Il7r* and *Tcf7* also enriched in Brca2^{null} tumors (Fig. 7a,c). Within the myeloid compartment, both pro-inflammatory TAMs and cDC1s were enriched in Brca2^{null} relative to Brca1^{null} tumors, consistent with our untreated analyses.

Taken together, our single cell analyses support the notion that the improved response to ICB observed in Brca2^{null} models and tumors may rely not only on T cells, but also on components of the innate immune system, and are observed in both the ICB-naïve and treated settings.

Discussion

Using human tumors and isogenic murine models, we show that BRCA1 and BRCA2 loss differentially modulate the tumor-immune microenvironment and response to checkpoint blockade immunotherapy. Prior data have described BRCA-mediated effects on the tumor-immune microenvironment. [40,48,49] However, to our knowledge, our study is the first to directly compare the effect of BRCA1 and BRCA2 loss on the microenvironment, and to provide evidence that they may have distinct consequences on tumor immunity and response to ICB.

Our results demonstrating lack of response to ICB in our Brca1^{null} pre-clinical ICB models, coupled with transcriptomic analysis, may help explain this important emergent paradox: although Brca1^{null} tumors have been classically described as harboring increased lymphocyte and T cell infiltration, [26,48,50–52] responses to ICB in patients with triple-negative breast cancer and *BRCA1* germline mutations have remained low. [53,54] These data imply that the increased T cell infiltration in Brca1^{null} tumors alone may not be enough to facilitate response to ICB and suggests pleiotropic effects of BRCA1-deficiency may drive immunoregulatory processes that limit response. [35]

Our analyses also suggest that BRCA2 deficiency is associated with increased immunogenicity, and improved response to ICB. The data suggest that there may be previously uncharacterized interactions between BRCA2 and the innate immune system mediated by NK, macrophage and dendritic cell populations. While several recent studies highlighted potential effects of BRCA deficiency on pro-inflammatory responses particularly with PARP inhibition, [55–58] here we make the observation that gene expression programs and immune cell populations related to innate immunity are specifically enriched in Brca2^{null} tumors relative to Brca1^{null} tumors. Although the exact mechanism of differential ICI sensitivity in *BRCA* mutant tumors are the subject of further investigation, our work highlights several potential mechanisms that may contribute. In particular, analysis of bulk and single cell RNA-sequencing from murine tumors revealed distinct immune landscapes. Multiple T cell phenotypes--including cytotoxic, memory, and exhausted populations--were enriched in Brca2^{null} tumors relative to Brca1^{null} tumors. In comparison, Brca1^{null} tumors were further associated with immunosuppressive myeloid populations that may inhibit cytotoxic T cell responses. These findings were detected in both the ICB-naïve and treated settings. Consistent with these data from mouse models, in human tumors, Brca1^{null} tumors were associated with up-regulation of an immuno-regulatory expression program including alternative checkpoints, that may result in additional ICI resistance mechanisms. Moreover, we found expression of multiple genes in immune-deficient tumor cell lines that may drive the differences in immune infiltration tumors, suggesting tumor-cell intrinsic differences between BRCA1and BRCA2 deficiency. Lastly, the differential mutational landscape associated with BRCA1- and BRCA2-deficient tumors on murine WGS and human WES may be associated with more immunogenic indel alterations and resulting potential neoantigens as well as decreased copy number changes associated with immunosuppression in *BRCA2*-mutant tumors. Our study warrants further exploration of the exact mechanisms by which *BRCA1* and *BRCA2* mutations may bring about different immune microenvironments and their respective interactions with the immune system more generally.

Furthermore, using a large pan-cancer cohort with germline and somatic targeted sequencing, we demonstrate an association between truncating mutations in *BRCA2*, but not *BRCA1*, and improved outcomes after ICB. While our clinical analysis remains exploratory, the data are consistent with multiple previous reports of improved response in BRCA2-deficient tumors and limited response with BRCA1-deficiency, [1,3,10,26,53,54,59,60] Some studies have considered *BRCA1* and *BRCA2* together or as part of a larger panel of DDR-related genes. [9] While definitive evidence will require prospective evaluation of ICB response in cohorts of patients with *BRCA1* and *BRCA2* mutations, our results have significant implications for the design of future clinical trials and highlight a possible fundamental difference in the mechanism by which these two canonical tumor suppressors mediate anti-tumor immunity.

Methods

Description of Patient Cohorts

As previously described, [16] after receiving institutional review board approval from the Memorial Sloan Kettering Cancer Center, institutional pharmacy records were used to identify patients who received at least one dose of immunotherapy (atezolizumab, avelumab, durvalumab, ipilimumab, nivolumab, pembrolizumab, or tremelimumab) and then cross-referenced with patients who had MSK-IMPACT testing done in the context of routine clinical care. MSK- IMPACT is a targeted panel that contains either 341, 410 or 468 genes depending on when the testing was performed although the majority of the patients in the analysis treated with immunotherapy were sequenced with the most recent 468 gene panel. The majority of patients who received MSK-IMPACT testing on tumor tissue are enrolled on an institutional IRB-approved research protocol (NCT01775072) with the remaining patients receiving testing as part of routine clinical care. Details of tissue processing and next generation sequencing and analysis have been previously described. [61,62] For the analyses presented in this study, we obtained next-generation sequencing data and associated clinical data for 24,459 patients available on the cBioportal. Identifiable germline data is available on patients consented to an optional part of the institutional protocol permitting germline analysis (N = 5,745). In order to comprehensively analyze the role of germline and somatic mutations in the entire cohort of patients treated with ICB, original sequencing files and relevant clinical data (overall survival from ICB administration) were anonymized by a third party without investigator access to the original patient identification. We analyzed 2185 patients treated with anti-CTLA4, anti-PD1, anti-PDL1, or a combination of all three drugs between 8/19/2010 and 4/4/2017. For assessment of treatment response only, patients in the germline consented cohort or patients with somatic mutations were used for analysis and MSI tumors were excluded. Patients who were deceased prior to receiving a diagnostic scan on ICB therapy (10 patients) or who did not have evaluable disease for response assessment (22 patients) were excluded from response analysis. Remaining patients had their responses independently assessed by three physicians, including 18 patients with truncating *BRCA2* mutations. Clinical benefit was defined as complete response, partial response or stable disease for greater than 6 months). Response assessment was performed by clinician review and independently validated. Due to small numbers of identifiable patients with *BRCA1*-mutations (n=9), responses for patients with *BRCA1* mutations were not analyzed. For TCGA analysis, patients with biallelic pathogenic germline mutations and somatic mutations from the breast cancer cohort were obtained as described previously. [37]

Somatic and Germline Mutation Assessment

For patients receiving MSK-IMPACT testing, those with and without truncating somatic mutations (defined as frameshift, intragenic, and nonsense mutations) in KEGG pathways were input into a Kaplan-Meier survival analysis. Mutations for analysis in Figure 1a were obtained using the previously described CLIA-certified MSK-IMPACT mutation pipeline based on Mutect.

[61,63] Mean coverage in target genes was 1,304X. To identify somatic single nucleotide variants (SNVs) in MSK-IMPACT data from raw data, we used a pipeline that integrates mutation calls from four different callers: MuTect 1.1.4, Strelka 1.0.3, SomaticSniper 1.0.4, and Varscan 2.3.7. [64]

All tools are used with parameters recommended by the authors and the union of all called mutations was used. Germline variants were determined using HaplotypeCaller, [65] and those with normal allele frequency <= 0.01 were filtered out of further analyses. Insertions and deletions were determined using Varscan and Strelka 1.0.3 with default settings. SNVs with an allele read count of less than 4 or with corresponding normal coverage of less than 7 reads were filtered out. Mutations are annotated using SnpEffect and SnpSift Version 4.3. [66] Indels with tumor allele frequency less than 0.04 were filtered out. The total number of somatic mutations identified was normalized to the exonic coverage of the respective MSK-IMPACT panel in megabases to calculate the TMB. Mutations in driver oncogenes were not excluded from the analysis. As a significant portion of patients who received ICB in the study did not consent to evaluation of germ-line DNA, we anonymized a subset of clinical data and BAM files and recalled somatic and germline variants using our standard mutation pipeline. For analysis of ICB-treated patients, we considered mutations to be likely pathogenic if they met one of the following three criteria: (1) a germline truncating or frame-shift mutation (2) germline variants curated by our institutional clinical genetics service as pathogenic (3) somatic mutations that are truncating or frame-shift. Detection of loss of heterozygosity (LOH) on MSK-IMPACT data was not performed due to reduced sensitivity secondary to limited heterozygous SNPs on the targeted panel. For all TCGA analysis, biallelic pathogenic mutations were identified as described previously. [37] Briefly, somatic mutations for each individual cancer were determined from mutation annotation files (MAF) obtained from Broad firehose (1/28/16). Germline variant in TCGA samples were detected with HaplotypeCaller from the Genome Analysis Toolkit (GATK v.3/3) in the gvcf mode with default settings, and only those detected both in tumor and normal tissue were retained. Additional details on germline pipeline analysis are available at https://github.com/rj67/germVar2. Allele specific copy number information was generated using ASCAT. Deletions were examined for microhomology along the deletion sites as calculated by counting the maximum number of matched sequences along the deleted site, compared with the deleted sequences. The following script (https://github.com/ipstone/modules/blob/master/summary/calc_delmh.py) with the respective human genome reference is used to calculate the microhomology sequences. The proportion of deletions with microhomology is obtained by dividing the number of deletions with microhomology sequences with the total number of deletions in the sample.

Gene Set Selection for IMPACT pathway analysis

For pathway analysis shown, KEGG gene sets (excluding cancer and disease genesets) obtained from MsigDB were filtered on genes contained within the MSK-IMPACT panel. Of note, 52 pathways out of 186 are represented by at least 2 genes in the pathway and characterized biological processes (rather than pathological states) and were used for analysis. Any patient with a truncating (stop gained or frameshift) mutation in any gene within the pathway was considered altered and log rank overall survival analysis was conducted from time of ICB administration between patients with a truncating alteration in the pathway vs. no alteration in the pathway.

Generation of Mouse cell lines

All cell lines were obtained directly from ATCC prior to experimentation. CRISPR-Cas9-nickase editing was performed according to a published protocol. [67] pSpCas9n(BB)-2A-GFP (PX461) was a gift from Feng Zhang (Addgene plasmid # 48140). Briefly, optimize guide RNAs were designed and clones into the PX461 plasmid (Brca2: GATACAATTCTGAACCTCCGG and GAAAGCTCCTCAAACCAATTG, Brca1: GACTCCTTCCCAGGACAACT and GTTCATGAATACTGCCCGAGC). Transient transfection was performed using GenJet (SignaGen) reagent according to manufacturer instructions and individual GFP positive cell were sorted into single wells containing culture medium. Single cell derived colonies were gradually expanded and screened for frameshift mutations in all alleles using targeted PCR of the locus followed by TOPO-TA cloning (Invitrogen) and sequencing of up to 20 colonies. Cells were maintained in culture for 3 additional months (4 months total) to allow phenotypic accumulation of mutations prior to sequencing and *in vivo* experiments.

Immunofluorescence and Quantification

Cells were plated at 50% confluence in chamber well slide overnight and sham treated (0 Gy) or irradiated using a Shepherd Mark-1 ^{137}Cesium irradiator to a dose of 10 Gy. After 4 hour incubation, cells were fixed in 2% paraformaldehyde and 0.1% Triton X-100 in PBS for 30 minutes at room temperature. Cells were washed with PBS and permeabilized with 0.5% Triton-X 100 in PBS for 10 minutes at room temperature followed by blocking with 10% calf serum for 1 hour at room temperature. rabbit anti Rad51 IgG (Calbiochem PC-130, 1:400 dilution), mouse anti-gH2AX IgG (Millipore Cat# 05–636, 1:500 dilutions) in humidified chamber 2 h at room temperature. Slides were washed 3 times and incubated with Alexa-fluor 488 conjugated goat anti-rabbit IgG (Molecular Probes/invitrogen, Carlsbad, CA 1.7 ug/ml, 1:1000), Alexa-fluor 594-conjugated goat anti-mouse IgG (Molecular Probes/invitrogen, Carlsbad, CA 1.7 ug/ml, 1:1000) for 1 hr at room temp followed by washing 3x and mounting with DAPI (ProLong Gold, Life Technology) according to manufacturer's instructions. Images were obtained using a Zeiss LSM 510 confocal microscope. Quantification was performed using CellProfiler to estimate the number of foci per nucleus and the percent of nuclei with greater than 5 foci were considered positive.

In vitro PARP sensitivity assay

Number of cells were quantified using Vi-cell (Beckman) and 500 4T1 parental or Brca2^{null} cells were plated in a 96 well plate with increasing concentrations of olaparib (AstraZeneca). After 96 hours the number of viable cells were quantified using CellTiter-Glo luminescent cell viability assay (Promega).

Karyotyping analysis

Cultures were treated with colcemid at a final concentration of 0.1 μg ml^{-1} for 45 min at 37 °C. The cultures were then trypsinized and resuspended in pre-warmed 0.075 M KCl followed by incubation for an additional 10 min at 37 °C and fixation in methanol:acetic acid (3:1). The fixed cell suspension was then dropped onto slides, stained in 0.08 μg ml^{-1} DAPI in 2×SSC for 5 min and mounted in antifade solution (Vectashield, Vector Labs). Metaphase spreads were captured using a Nikon Eclipse E800 epifluorescence microscope equipped with GenASI Cytogenetic suite (Applied Spectral Imaging). Chromatid breaks were counted as single break events, exchanges resulting in tri-radials/quadri-radials as two break events, and other complex exchanges were converted into the minimum number of breaks required for their theoretical reconstruction. Since the baseline karyotype in the parental lines were highly abnormal and heterogenous, chromosome-type aberrations were not scored.

Whole genome sequencing of murine tumor cell lines

For isogenic mouse models (4T1-parental, 4T1- Brca2^{null}, 4T1- Brca1^{null}), samples were cultured for four months followed by isolation of individual single-cell clones and expansion for sequencing. DNA was extracted and sequenced at 74 – 106x (median 80x) coverage. FASTQ files were aligned to MM10 mouse reference with bwamem v0.7.15. Somatic mutations were called with VarScan v2.4.3, Strelka v2.9.10, Platypus 0.8.1, Mutect2 (part of GATK 4.1.4.1) and SomaticSniper 1.0.5.0 (for SNVs only). DNA from a 4T1 parental single-cell clone at time 0 was used as normal. For SNVs, the following filtering parameters were applied: called by at least 2 callers, covered by more than 50 reads in tumors and more than 7 reads in normals, with >10 reads supporting the mutation, mutant allele fraction (MAF) ≥10%, and less than 1% reads supporting the mutation in the normal (Tcov > 50 & Tac > 10 & Taf >= 0.1 & Ncov > 7 & Naf <= 0.01). Indels were filtered firstly in the same way as SNVs, and then further filtered by those identified by at least 3 callers. Indels reside in the blacklisted regions (https://www.encodeproject.org/annotations/ENCSR636HFF/), and low mappability regions (such as repeat maskers) are excluded. Mouse isogenic samples' 96 base substitution profiles were calculated with the trinucleotideMatrix function from the maftools package. Background mutation profiles (average from the 4T1-parental controls) were subtracted from Brca1^{null} and Brca2^{null} samples' profiles. [19] After background subtraction, the resulting mutation profiles were further adjusted by multiplying the trinucleotide context ratio between the human genome (hg19) and mouse genome (MM10). The resulting SNV 96 channel mutation profiles were finally compared within subclones or COSMIC Signature-3 by calculating the cosine similarity using the cos_sim_matrix function from the mutationalPatterns package. [68] Deletions were examined for microhomology along the deletion sites as calculated by counting the maximum number of matched sequences along the deleted site, compared with the deleted sequences. The following script (https://github.com/ipstone/modules/blob/master/summary/calc_delmh.py) with the respective mouse genome reference is used to calculate the microhomology sequences. The proportion of deletions with microhomology is obtained by dividing the number of deletions with microhomology sequences with the total number of deletions in the sample.

Mouse experiments

For the breast cancer model, 1×10^5 4T1 cells in 50 μl of PBS were injected into the mammary fat pad of 6–7 week old female Balbc/J mice (Jackson Laboratories) under isofluorane or ketamine anesthetic along with analgesics. For the colorectal cancer model, 2×10^5 CT26 cells in 100 μl of PBS were injected into the left flanks subcutaneously of 6–7 week old female Balbc/J mice (Jackson Laboratories). Mice with clinically palpable tumors (2 mm in diameter) were randomized into indicated treatment arms. IgG (2A3, Bioxcel, 100μg), anti-Pd-1 (RMP1–14, Bioxcel 100μg), or anti-Ctla4 (9H10, Bioxcel 250μg), antibodies were administered intraperitoneally in 100 μl of PBS twice weekly (q3–4 days). Tumor volumes were measured twice weekly using calipers and calculated by the formula: $\frac{(Length)\ x\ (Width)^2}{2}$. All mouse experiments shown were repeated at least twice to ensure reproducibility. Mice were euthanized by carbon dioxide prior to necropsy.

Quantitative RT-PCR

cDNA was generated from RNA extracted from cell lines and tumors using Ecodry premix (Takeda). Conventional QPCR experiments were performed using FastStart Universal SYBR Green Master mix (Roche). Taqman QPCRs were performed using PrimeTime qPCR master mix (IDT). For detection of the Brca2 WT allele mRNA by conventional QPCR, the forward primer was designed to overlap with the common deletion region of all Brca2 KO alleles. For detection of the Brca2 WT allele mRNA by Taqman QPCR, the primer pair was designed to flank the deletion region while the probes were designed to overlap with the common deletion region. Sequences of all QPCR primers and probes are provided in Supplementary Table 6.

Western blotting

For validation of Brca1 knockout, immunoblotting was performed using Bio-Rad Trans-Blot system according to manufacturer instructions. Briefly, cell lysates were generated from cell lines using CelLytic M (Sigma) and sonicated in a water bath for 10 minutes. After centrifugation, supernatant were mixed with loading dye containing 2-mercaptoethanol and loaded onto precast Novex 4–12% Bis-Tris gels and run for approximately 90 minutes at 180 V. Transfer was performed overnight at 40 V to PVDF membranes and blocked with 5% milk, followed by overnight incubation with primary antibodies (BRCA1 R&D MAB22101, Vinculin Sigma V4505) and 1 hour secondary incubation. Full unedited images are available as Supplementary Figure 1.

Flow cytometry

Tumors were resected at 14 days post-tumor injection and dissociated into single cell suspensions using a gentle MACS tissue dissociator and mouse Miltenyi Mouse Tumor Dissociation Kit according to manufacturer instructions (Miltenyi Biotech). Cell suspensions were stained using murine Live-Dead zombie aqua fixable marker followed by surface antibodies. Stained single cell suspensions were analyzed using the Fortessa (BD) flow cytometric analyzer. Quantitative data analysis was performed using Flowjo software (Treestar). All experiments were repeated at least twice.

Immunofluorescence

Resected tumors at 14 days were fixed in formalin at room temperature overnight and transferred to 70% ethanol at 4 °C. Tumors were embedded in paraffin and sectioned onto glass slides. Staining was performed by the Molecular Cytology Core Facility at MSKCC using CD3-Alexa647, CD4-Alexa488, CD8-Alexa546 and CD45-Alexa 594. Slides were subsequently stained using a Mirax scanner for downstream analysis and quantification. Number of cells per high powered field was quantified by a reviewer blinded to treatment arm in 5 fields per condition spanning 4–5 tumors.

Bulk RNA-Seq Analysis of murine and human tumors

For mouse tumors, fresh frozen tissue from day 14 tumors were used for isolation of DNA and RNA and submitted to the Integrated Genomic Core for library preparation and sequencing. 3–5 replicates per condition were submitted for sequencing depending on RNA quality. For TCGA BRCA cohort, FASTQ files were downloaded from GDC and aligned against the hg19 assembly by STAR, and murine data was aligned to the mm10 assembly. Gene level count values were then computed by the summarizeOverlaps function from the R package “GenomicAlignments” with UCSC hg19 KnownGene (or mm10, for murine data) as the base gene model. The Union counting mode was used and only mapped paired reads were considered. Only genes with count > 1 were considered for downstream analysis. Differentially Expressed Genes (DEG) analyses were also done by DESeq2. [69] Briefly, DESeq utilizes a generalized linear model with the Wald statistical test, with the assumption that the underlying gene expression count data following a negative binomial distribution. To correct possible unknown batch effect, surrogate variables were computed by the R “sva” package and included as covariates in the DEG analysis. [70] Pathway analysis over DEG genes was conducted using the GOSeq package and Ingenuity Pathway Analysis (IPA) (QIAGEN Inc., https://www.qiagenbioinformatics.com/products/ingenuity-pathway-analysis). Immune deconvolution analysis was performed on RNA-seq data (FPKM) from breast cancer patients using single-sample gene set enrichment (ssGSEA) with previously defined immune cell subset signatures, using normalized gene-level RNA-seq data from TCGA. [71] Specifically we determine the ssGSEA values for each of 21 immune cell populations. Subsequently, principal component analysis on these 21 cell populations was performed and the first 2 components were graphed. Following principal component analysis of immune deconvolution scores, we tested for significant separation between BRCA1 mutant and BRCA2 mutant samples using the permutational multivariate analysis of variance (PERMANOVA) method. Given an ordination (i.e. PCA) and pre-defined groups (e.g. BRCA1 mutant and BRCA2 mutant), the PERMANOVA method tests the null hypothesis that there is no difference between the positions of the centroids of each group. [72] Under the null, any difference between the positions of the centroids of each group (e.g. BRCA1 mutant or BRCA2 mutant) would be obtained even if each sample were randomly assigned to a group through permutation. [73]

Single-cell RNA-seq analysis

For mouse single cell analysis, orthotopic implanted tumors in the mammary fat pad were isolated at day 12 after implantation. Single cell suspensions were generated from 2 pooled tumors using the Mouse Tumor Dissociation Kit according to manufacturer instructions (Miltenyi Biotech). Single cell library preparation was performed according to manufacturer instructions using the mouse single cell RNAseq kit (10X genomics).

For scRNA analysis, we followed the same pre-processing procedure for both ICB-untreated and ICB-treated tumors. Fastq files for *Brca1* and *Brca2*-deficient cells as well as parental cells were aligned and pre-processed to produce a count matrix using 10X Cell Ranger version 3.0.2. The resulting count matrix was then filtered to exclude all cells with UMI count in mitochondrial genes > than 20% of all counts as described in Azizi *et al* Cell 2018, and all ribosomal genes were also removed from the analysis. [11] We further filtered any genes that had a mean log count <= 2.5 to reduce sparsity in the final count matrix. Following these initial filtering steps, we used Seurat version 2.4 to scale the UMI counts and perform log normalization of the data. [74,75] To mitigate batch effects, we adopted a stringent approach whereby each replicate in each condition was treated as a separate batch. Log-normalized counts for each sample were used as input to the mnnCorrect method Haghverdi *et al* 2018 from the scran package. [76] The batch-corrected PCA from mnnCorrect was used as input to Phenograph clustering[43] at resolution 1.0 and t-SNE [77] to produce the plot shown in Fig. 5a. The number of biological replicates for ICB-untreated mice were 2 for Brca1 null (17QQ2/QQ3), 3 for Brca2 null (21E1, 21E2, 21E3), and 3 for wildtype (parental; PAR1, PAR2, PAR3). The number of biological replicates for ICB-treated mice were 2 each for Brca1 null, Brca2 null, and wildtype. Differential expression analyses were conducted using the FindMarkers function in Seurat, using the negative binomial likelihood ratio test. To further discern the range of phenotypes among ICB-untreated myeloid populations, we reclustered all Cd3- Cd14+ cells from Fig. 5a at a resolution of 0.6. Cluster proportions were then evaluated as a percentage of all cells or as a percentage of T cells and myeloid cells separately. Since the cluster enrichment data are compositional, P-values for enrichments in Brca1 null or Brca2 null tumors were calculated using Fisher's exact test.

Microarray Analysis

Raw data for the METABRIC dataset was obtained from cBioPortal. Differential gene expression analysis between patients with BRCA1 and BRCA2 mutations was conducted in R using the Limma package, version 3.36.2.

Copy Number Analysis

Copy number analysis was performed on TCGA exomes using FACETS v0.5.0. [78] The fraction of the copy number altered genome was defined as the fraction of the genome with either non-diploid copy-number or evidence of loss of heterozygosity.

In silico Neoantigen Prediction Pipeline

All nonsynonymous point mutations identified were translated into strings of 17 amino acids with the mutant amino acid situated centrally using a bioinformatic tool called NAseek. [44] A sliding window method was used to identify the 9 amino acid substrings within the mutant 17mer that had a predicted MHC Class I binding affinity) of the patient-specific HLA alleles determined by Polysolver. [4,79] Binding affinity for the mutant and corresponding wild type nonamer were analyzed using NetMHCpanv4.0 software. [80]

Statistics and reproducibility

All pairwise group comparisons were performed with the Wilcox-rank sum test. We performed survival analyses using the Kaplan-Meier estimator. The log-rank test was used to determine statistical significance of the survival distributions between groups. Hazard ratios were computed using univariate or multivariable Cox regression. False discovery rates were adjusted using the Benjamini-Hochberg procedure in R. All survival analyses analysis were performed using the survival package in R. Single cell RNA-seq cluster proportions were compared using Fisher's exact test. Sample size for mouse experiments were chosen to provide sufficient power given expected tumor size variability based on experience. No statistical method was used to predetermine sample size. No data were excluded from the analyses. Randomization was performed in mouse experiments between treatment groups. Where possible, investigators were blinded to allocation during objective outcome assessment including tumor size measurement, immunofluorescence quantification, and clinical immunotherapy response assessment.

Further information on research design is available in the Nature Research Reporting Summary linked to this article.

Code Availability Statement

No custom code was used for the analysis. Code will be made available upon reasonable request.

Data Availability Statement

Bulk RNA sequencing from murine tumors and cell lines as well as murine single cell RNA sequencing data that support the findings of this study have been deposited in the Gene Expression Omnibus (GEO) and Sequence Read Archive (SRA) under accession codes GSE137818 (all murine bulk RNA sequencing, and ICB-untreated single cell RNA sequencing) and PRJNA632854 (whole genome sequencing and ICB-treated single cell RNA sequencing). Previously published somatic genomic data that were re-analyzed here are available at https://www.cbioportal.org/study/summary?id=tmb_mskcc_2018.

Human data that were derived from the TCGA Research Network are available from http://cancergenome.nih.gov/. Germline data is available via dbGAP under accession code phs000178.v11.p8. Details of which exact TCGA cases were analyzed in the present study are available in the source data for Figure 4. Processed data based for all datasets include murine and human variant calls, differentially expressed genes for bulk and single cell RNA sequencing datasets, and GSEA outputs for bulk RNA sequencing analyses. A detailed description of the data available in supplementary and source data follows below.

In general, GSEA outputs for all bulk RNA sequencing analyses are included in Supplementary data, with the exception of differentially expressed genes for Brca2^{null} and Brca1^{null} tumors in culture (analysis in Figure 3 and Extended Data Figure 5), which are also included in Supplementary Table 3.

Source data are included for Figures 1–7, and Extended Data Figures 3–8, and Extended Data Fig. 10. SNVs and indels for murine whole genome sequencing data can be found in

Source Data for Figure 2 and Extended Data Figure 3. Differentially expressed genes between murine ICB untreated Brca2 null and Brca1 null tumors are in Source Data for Figure 3 and Extended Data Figure 5.

Source Data for Figure 5–6 and Extended Data Figure 8 includes differentially expressed genes for ICB-untreated single cell RNA seq clusters. Source data for Figure 7 and Extended Data Figure 10 includes differentially expressed genes for ICB-treated single cell RNA seq clusters. Source data for Extended Data Figure 4 includes differentially expressed genes between murine ICB untreated Brca2 null and wildtype (parental) tumors. Source data for Extended Data Figure 6 includes differentially expressed genes between murine ICB-treated Brca2 null and Brca1 null tumors. Source data for Figure 7 includes mutations and copy number alterations in TCGA BRCA1/2 mutant samples. All other data supporting the findings of this study are available from the corresponding author on reasonable request.

Extended Data

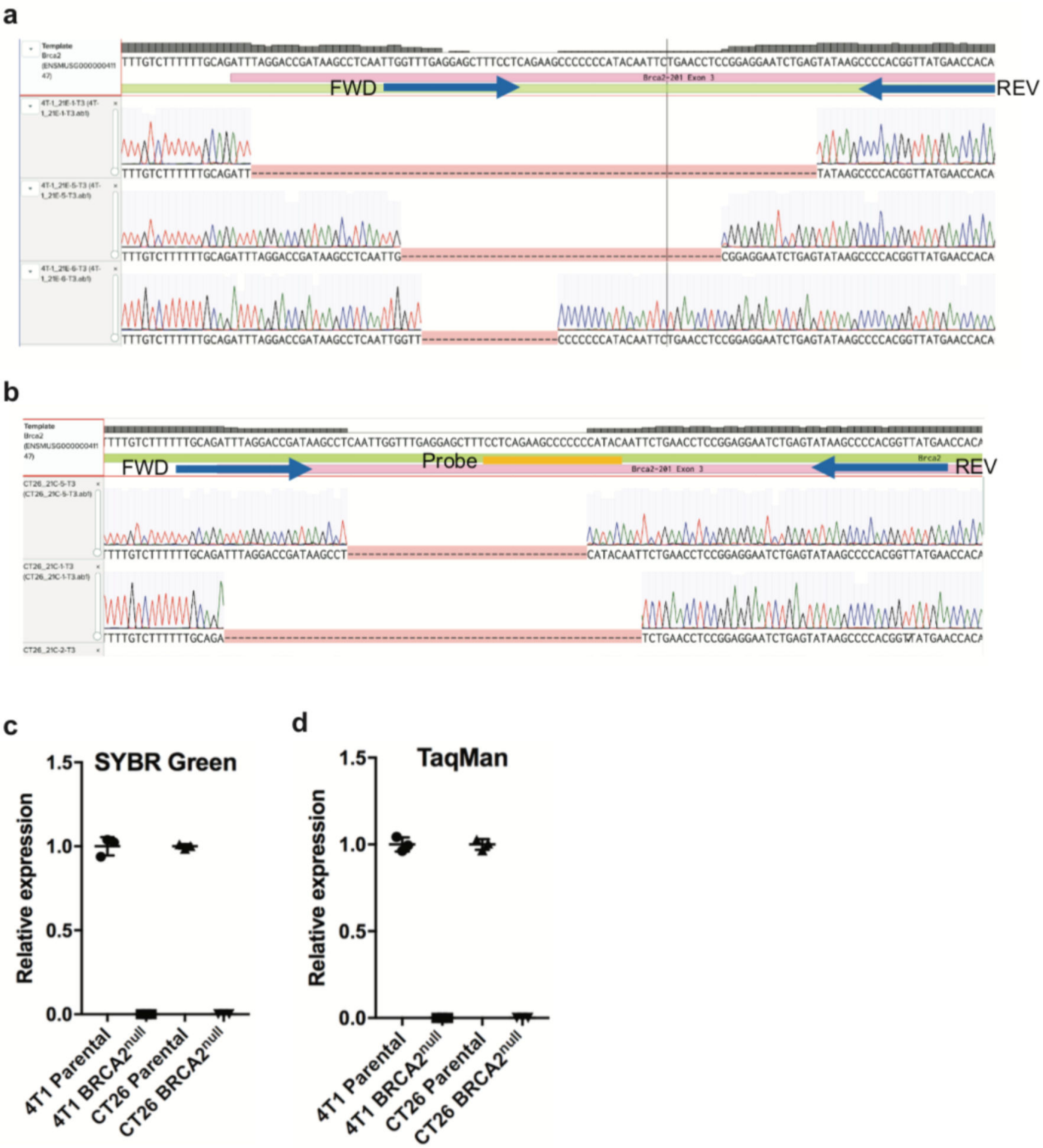

Extended Data Fig. 1|. Sequence traces of Brca2^{null} cell lines demonstrating frameshift mutations in all alleles.

PCR amplification and TOPO-TA cloning of individual allele copies was performed surrounding the CRISPR target guide sites to confirm that all alleles contain a frameshift or truncating mutation in Exon 3 of 4T1 Brca2^{null} **a**, and CT26 Brca2^{null} **b**, cell lines. Arrows indicate primer or probe locations. **c-d**, qRT-PCR amplication of *Brca2* WT-specific allele in cDNA generated from RNA isolated from cell lines using SYBR green based assay (c) and TaqMan based assay (d), n=3 technical replicates for **c** and **d**. Data are presented as mean values +/− SD

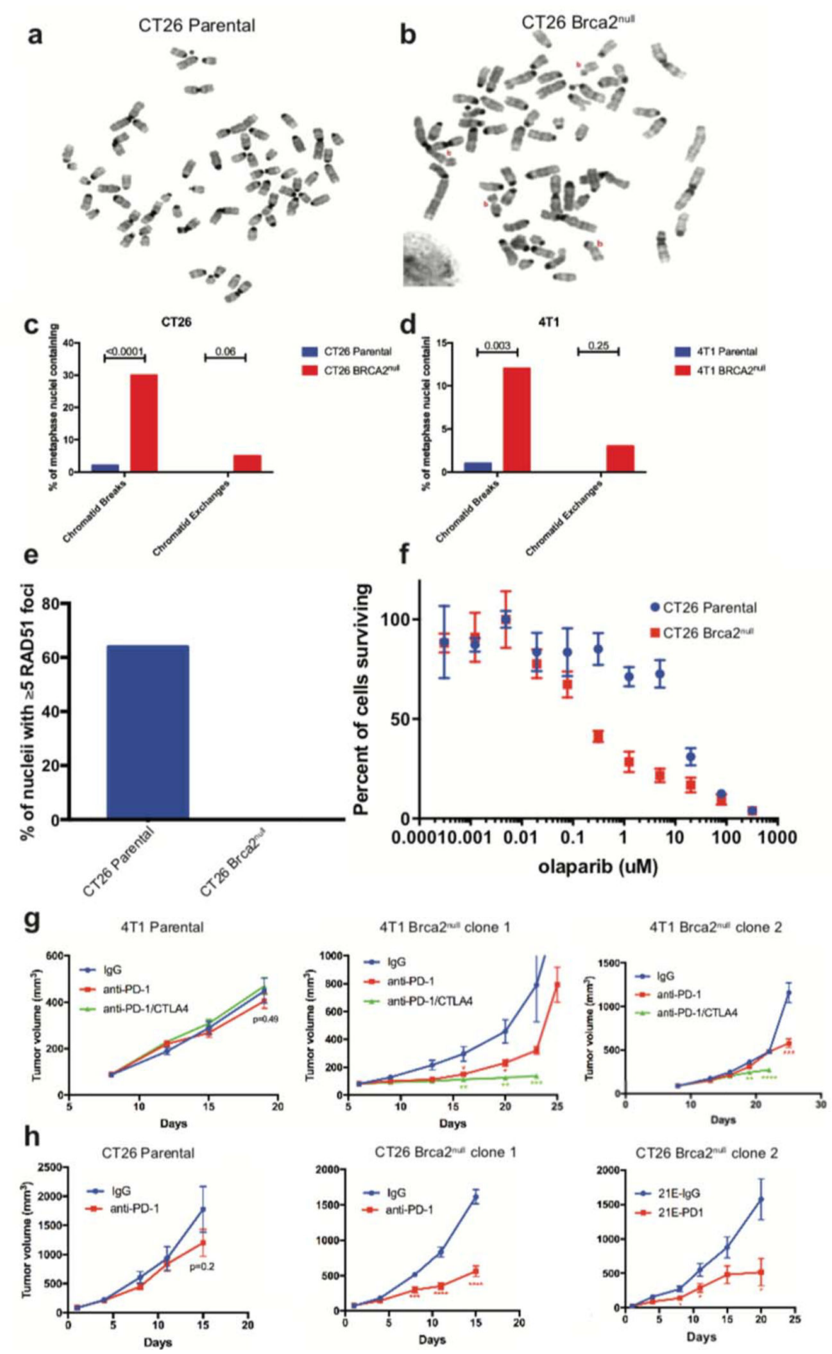

Extended Data Fig. 2 |. Characterization of the Brca2^{null} cell line.

a-b Representative images of parental (a) and Brca2^{null} (b) CT26 cell karyotype analysis demonstrating increased double strand breaks. **c,** Quantification of karyotype analysis shown in **a** representing n=100 metaphases analyzed demonstrating the percent of metaphase nuclei containing at least 1 of indicated abnormality. **d,** Quantification of karyotype analysis in 4T1 cells shown in Fig 2D representing n=100 metaphases analyzed demonstrating the percent of metaphase nuclei containing at least 1 of indicated abnormality. **e,** Quantification of immunofluorescent images of parental and Brca2^{null} CT26 murine colorectal adenocarcinoma cells 4 hours after 10 Gy irradiation stained with DAPI and antibodies to Rad51 and gamma-H2ax. **f,** *In vitro* relative viable cell count of parental and Brca2^{null} CT26 cell lines in the presence of PARP inhibitor olaparib at indicated concentrations after 96 hours in three independent assays in technical triplicate. Data are presented as mean values +/− SEM. **g-h**, Tumor growth curve of parental and additional Brca2^{null} clones with ICB treatment in both the 4T1(g) and CT26 models (h). (* $p<0.05$, ** $p<0.005$,*** $p<0.0005$, **** $p<0.00005$). All p values represent two-sided unpaired t test at respective timepoint. Data are presented as mean values +/− SEM

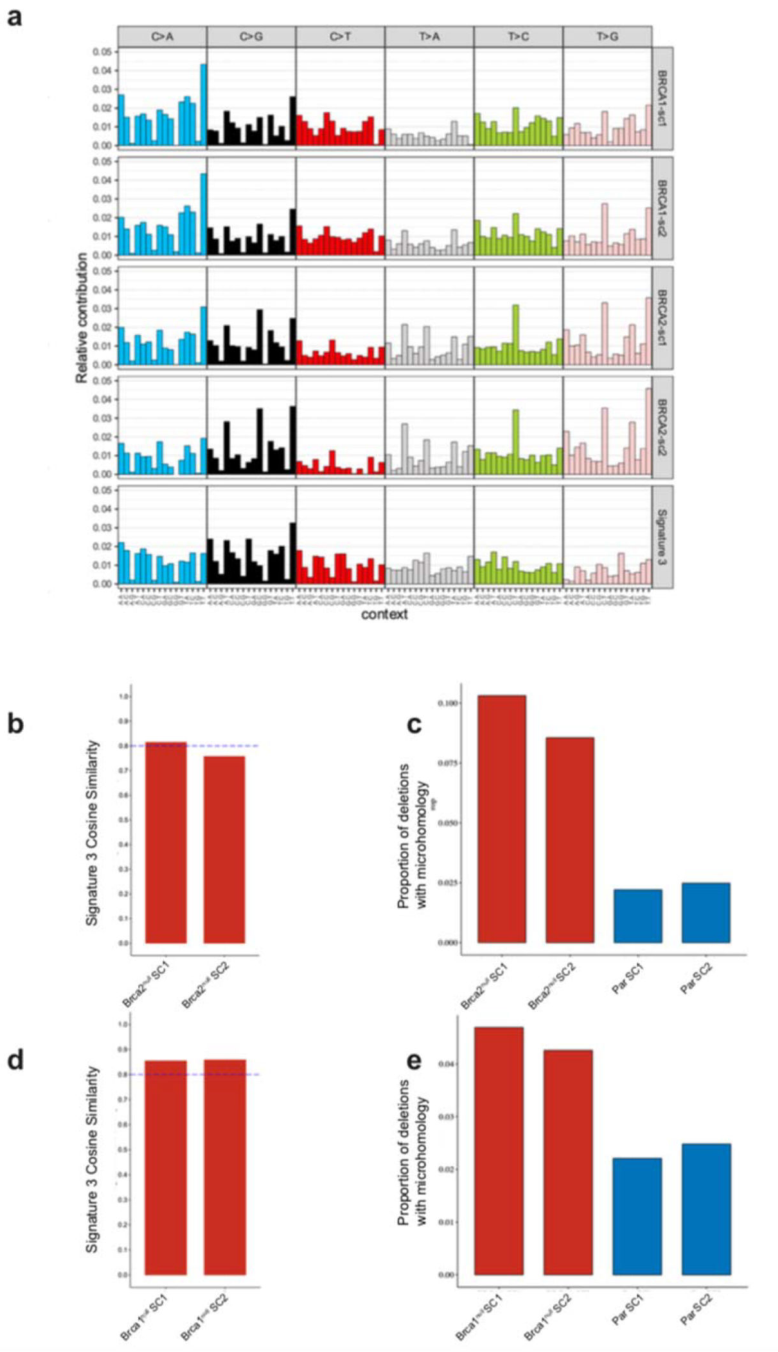

Extended Data Fig. 3 |. Characterization of the genomic alternation in 4T1 Brca2^{null} clones.

a, The 96 base substitution pattern for Brca2^{null} and Brca1^{null} single-cell clones after subtraction of background mutagenesis pattern derived from parental clones. Signature 3, previously associated with HRD (i.e. Signature 3), is provided for reference. **b**, Cosine similarity of BRCA2-null experimentally derived mutational signature to previously described mutational signature related to COSMIC Signature 3. **c**, Proportion of deletions with microhomology in 4T1 Brca2^{null} single-cell clones compared to parental single clones (two-sided Fisher's exact test P<0.0001, for all mutant single cell clones compared to parental). **d**, Cosine similarity of Brca1^{null} experimentally derived mutational signature to previously described mutational signature related to COSMIC Signature 3. **e**, Proportion of deletions with microhomology Brca1^{null} single-cell clones compared to parental single clones using a two-sided Fisher's exact test P<0.0001, for all mutant single cell clones compared to parental).

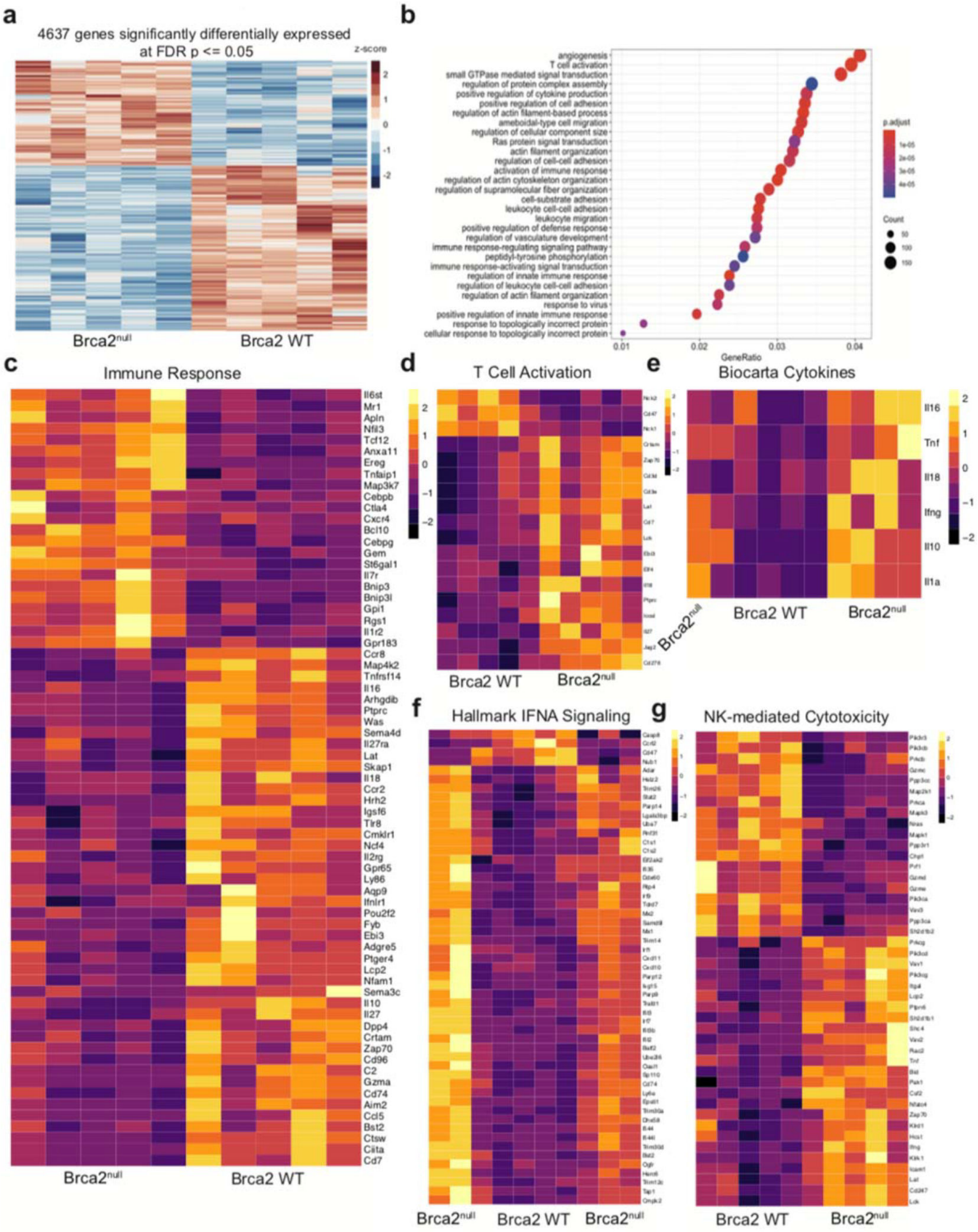

Extended Data Fig. 4 |. Bulk RNA-seq analysis between untreated Brca2^{null} and WT tumors yields gene expression programs related to adaptive and innate immune activation enriched in Brca2^{null} tumors.

a, Heatmap displaying all 4,637 genes significantly differentially expressed (FDR < 0.05) between untreated Brca2^{null} and Brca2-WT murine tumors from the 4T1 model. Data show drastic gene expression changes upon Brca2 inactivation *in-vivo*. P-values calculated from two-sided differential expression analysis using DESeq2 (Wald test) and corrected for multiple testing using the Benjamini-Hochberg method **b,** Pathway analysis on genes from **a** using GO pathways. Top enriched pathways in either Brca2^{null} or Brca2^{WT} tumors are shown. Color gradient of red to purple indicates decreasing adjusted p-value; circle size indicates number of genes in pathway. GeneRatio on x-axis indicates number of significantly differentially expressed genes from RNA-seq overlapping with genes in each pathway. P-values for overlap between input genes and pathway genesets calculated via two-sided hypergeometric test and corrected for multiple comparisons using the Benjamini Hochberg method. **c,** Heatmap showing significantly differentially expressed genes (FDR P <= 0.05, two-sided Wald test from DESeq2) between Brca2^{null} and WT tumors from the Immune Response pathway. **d,** Heatmap showing significantly differentially expressed genes (FDR P <= 0.05, two-sided Wald test from DESeq2) between Brca2^{null} and WT tumors from the T cell activation pathway. **e,** Heatmap showing significantly differentially expressed genes (FDR P <= 0.05, two-sided Wald test from DESeq2) between Brca2^{null} and WT tumors from the Biocarta cytokines pathway. **f,** Heatmap showing significantly differentially expressed genes (FDR P <= 0.05, two-sided Wald test from DESeq2) between Brca2^{null} and WT tumors from the Hallmark IFNA Signaling pathway. **g,** Heatmap showing significantly differentially expressed genes (FDR P <= 0.05, two-sided Wald test from DESeq2) between Brca2^{null} or Brca2^{WT} tumors from the NK-mediated cytotoxicity pathway. For **c-g**, P-values calculated from two-sided differential expression analysis using DESeq2 (Wald test) and correct for multiple testing using the Benjamini-Hochberg method.

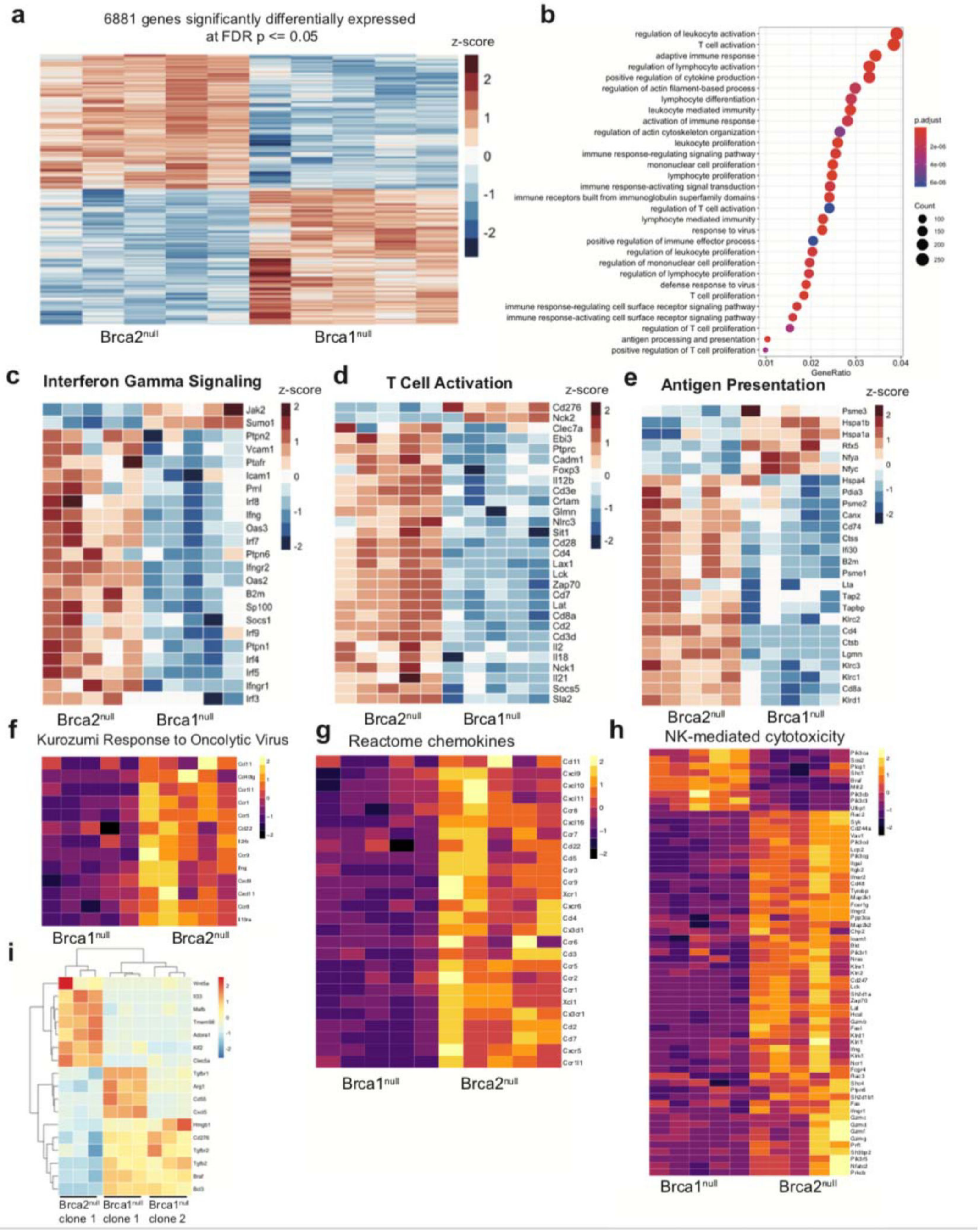

Extended Data Fig. 5 |. Bulk RNA-seq analysis between untreated Brca2^{null} and Brca1^{null} tumors yields gene expression programs related to adaptive and innate immunity enriched in Brca2^{null} tumors.

a, Heatmap displaying all 6,881 genes significantly differentially expressed (FDR < 0.05) between untreated Brca2^{null} and Brca1^{null} murine tumors from the 4T1 model. Data show drastic gene expression changes upon Brca2 inactivation. P-values calculated from two-sided differential expression analysis using DESeq2 (Wald test) and corrected for multiple testing using the Benjamini-Hochberg method. **b,** Pathway analysis on genes from **a** using GO pathways. Top enriched pathways in either Brca2^{null} or Brca1^{null} tumors are shown. Color gradient of red to purple indicates decreasing adjusted p-value; circle size indicates number of genes in pathway. GeneRatio on x-axis indicates number of significantly differentially expressed genes from RNA-seq overlapping with genes in each pathway. P-values for overlap between input genes and pathway genesets calculated via two-sided hypergeometric test and corrected for multiple comparisons using the Benjamini Hochberg method. **c,** Heatmap for genes significantly differentially expressed in **a** associated with interferon gamma signaling between Brca2^{null} and Brca1^{null} murine tumors from the 4T1 model. **d,** Heatmap displaying for genes significantly differentially expressed in **a** associated with T cell activation between Brca2^{null} and Brca1^{null} murine tumors from the 4T1 model. **e,** Heatmap for genes significantly differentially expressed in **a** associated with antigen presentation between Brca2^{null} and Brca1^{null} murine tumors from the 4T1 model. **f,** Heatmap showing significantly differentially expressed genes (FDR P <= 0.05) between Brca2^{null} and Brca1^{null} tumors from the Kurozumi Response to Cytolytic Virus pathway, evaluated using GSEA (FDR P <= 0.05). **g,** Heatmap showing significantly differentially expressed genes (FDR P <= 0.05) between Brca2^{null} and Brca1^{null} tumors from the Reactome chemokines pathway, evaluated using GSEA (FDR P <= 0.05).**h,** Heatmap showing significantly differentially expressed genes (FDR P <= 0.05) between Brca2^{null} and Brca1^{null} tumors from the NK-mediated cytotoxicity pathway, evaluated using GSEA (FDR P <= 0.05). For **c-h**, P-values calculated from two-sided differential expression analysis using DESeq2 (Wald test) and correct for multiple testing using the Benjamini-Hochberg method. **i**, Heatmap of mean log-normalized expression of differentially expressed genes for genes promoting immune activity/evasion in between Brca1^{null} and Brca2^{null} deficient cell lines in vitro. For all GSEA analyses, p-values calculated using two-sided pre-ranked analysis using log fold changes as input.

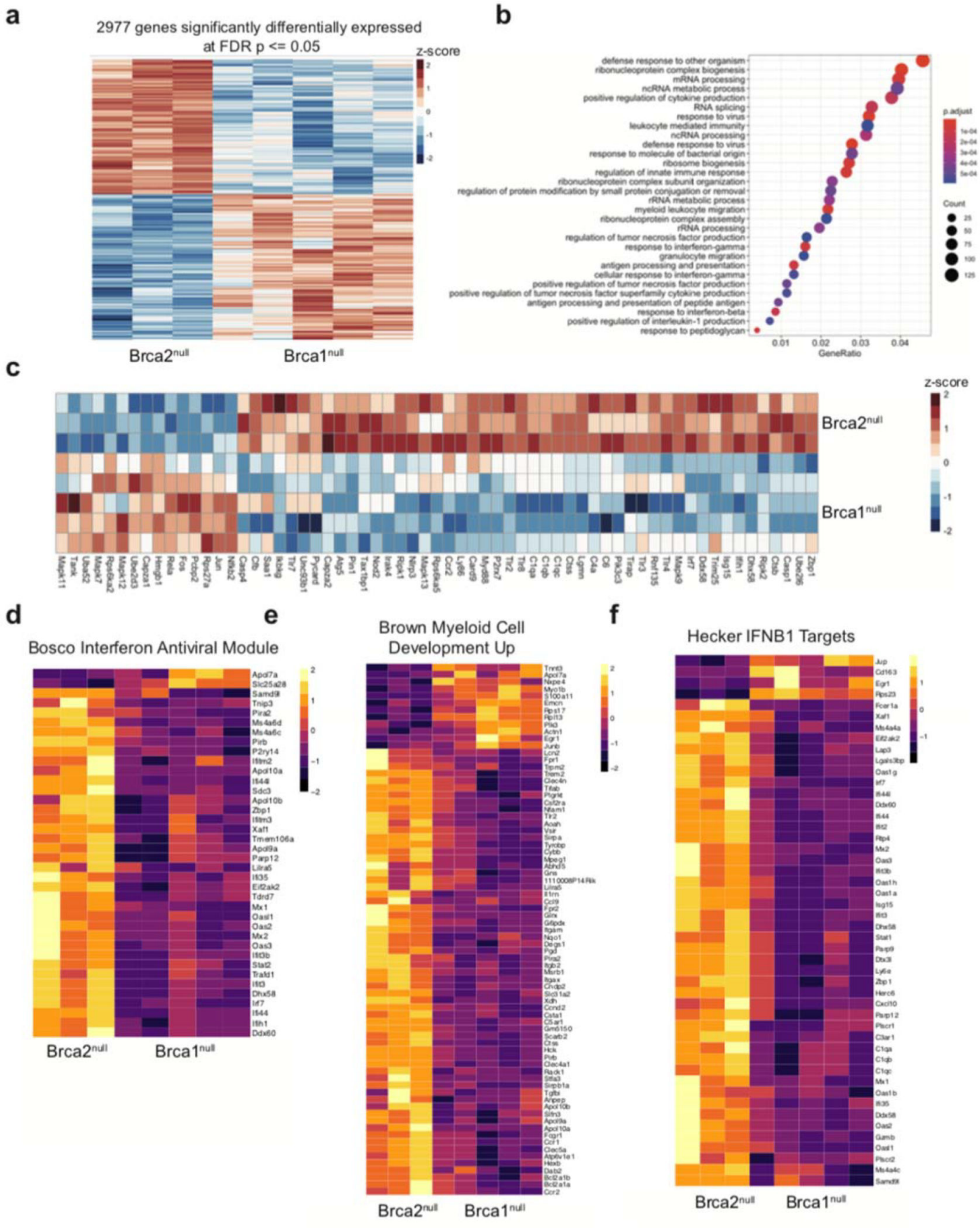

Extended Data Fig. 6 |. Bulk RNA-seq analysis between Brca2^{null} and Brca1^{null} tumors after treatment with anti-PD1 yields gene expression programs related to adaptive and innate immune activation enriched in treated Brca2 null tumors.

a, Heatmap displaying all genes significantly differentially expressed (FDR < 0.05) between Brca2^{null} and Brca1^{null} murine tumors from the 4T1 model after treatment with anti-PD1. Data show drastic gene expression changes upon Brca2 inactivation with treatment. P-values calculated from two-sided differential expression analysis using DESeq2 (Wald test) and corrected for multiple testing using the Benjamini-Hochberg method. **b,** Pathway analysis on genes from **a** using GO pathways. Top enriched pathways in either treated Brca2^{null} or treated Brca1^{null} tumors are shown. Color gradient of red to purple indicates decreasing adjusted p-value; circle size indicates number of genes in pathway. GeneRatio on x-axis indicates number of significantly differentially expressed genes from RNA-seq overlapping with genes in each pathway. P-values for overlap between input genes and pathway genesets calculated via hypergeometric test and corrected for multiple comparisons using the Benjamini Hochberg method. **c,** Heatmap displaying genes significantly differentially expressed in **a** associated with innate immunity between treated Brca2^{null} and Brca1^{null} murine tumors from the 4T1 model. **d,** Heatmap showing significantly differentially expressed genes (FDR $P <= 0.05$) between Brca2^{null} and Brca1^{null} tumors from the Bosco interferon antiviral module pathway, evaluated using GSEA (FDR $P <= 0.05$). **e,** Heatmap showing significantly differentially expressed genes (FDR $P <= 0.05$) between Brca2^{null} and Brca1^{null} tumors from the Brown myeloid cell development up pathway, evaluated using GSEA (FDR $P <= 0.05$). **f,** Heatmap showing significantly differentially expressed genes (FDR $P <= 0.05$) between Brca2^{null} and Brca1^{null} tumors from the Hecker IFNB1 targets pathway, evaluated using GSEA (FDR $P <= 0.05$). For **c**-**f**, p-values calculated from two-sided differential expression analysis using DESeq2 (Wald test) and correct for multiple testing using the Benjamini-Hochberg method. For all GSEA analyses, p-values calculated using two-sided pre-ranked analysis using log fold changes as input.

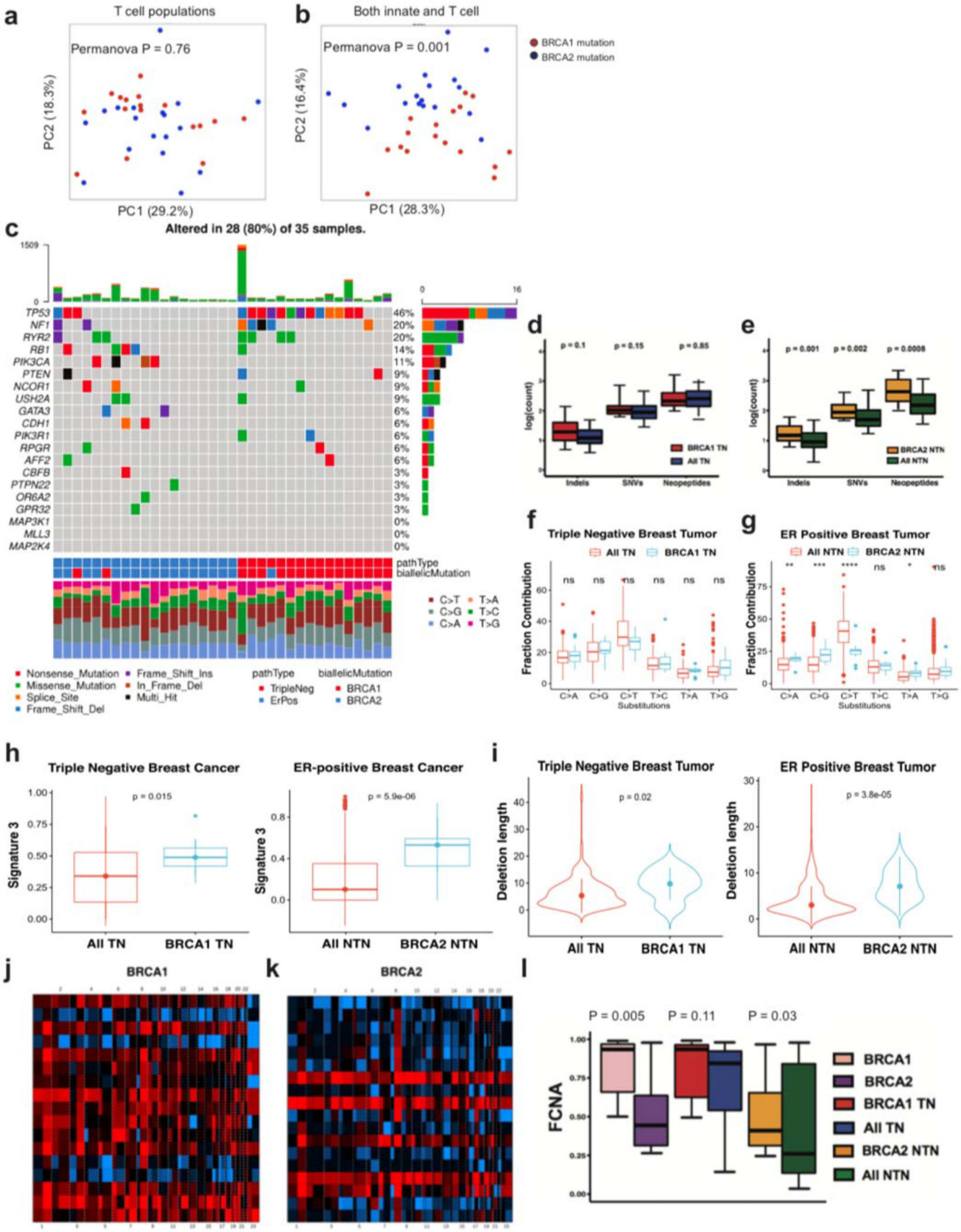

Extended Data Fig. 7 |. Whole exome sequencing analysis of *BRCA2*-mutant and *BRCA1*-mutant tumors from the TCGA breast cancer cohort

a, Principal component analysis (PCA) of ssGSEA scores for T cell populations for patients with either *BRCA1* or *BRCA2* germline or somatic biallelic mutations. P-value computed on separation between *BRCA1* mutant and *BRCA2* mutant samples using a two-sided PERMANOVA test. **b,** Principal component analysis (PCA) of ssGSEA scores for T cell populations for patients with either *BRCA1* or *BRCA2* germline or somatic biallelic mutations. P-value computed on separation between *BRCA1* mutant and *BRCA2* mutant samples using a two-sided PERMANOVA test. **c.** Oncoprint for 35 breast cancers with biallelic *BRCA1* or *BRCA2* mutations. Mutations in the top 20 most frequently mutated genes in breast cancer are illustrated, along with the mutational profile of each individual tumor. **d,** Comparison of indel, SNV, and neopeptide counts between triple negative *BRCA1*-mutant tumors (BRCA1 TN n=15, individual patients) vs all triple negative (All TN, n=153, individual patients) tumors. Data show no difference in mutation counts between *BRCA1*-mutant tumors and histology-matched control tumors. P-values calculated using two-sided Wilcoxon test, which is also used in e-i and l. For all the boxplot in this figure pannels **d-h** and **l**, the minima, maxima are plotted as the whiskers, 1st and 3rd quartiles are plotted as the bounds of the boxes, and medians are plotted as the center. **e,** Comparison of indel, SNV, and neopeptide counts between non-triple negative *BRCA2*-mutant tumors (BRCA2 NTN, n=17, individual patients) vs all non-triple negative (All NTN, n=700, individual patients) tumors. The same groups of patients, All TN (n=153), BRCA1 TN (n=15), ALL NTN (n=700), BRCA2 NTN (n=17) are used in the figure panel **d-h** and **l**. Data show increased levels of all alterations in *BRCA2*-mutant tumors compared to histology-matched control tumors. P-values calculated using two-sided Wilcoxon test. **f,** Comparison of fraction contribution of the six SNV substitutions between triple negative *BRCA1*-mutant tumors vs all triple negative tumors. P-values calculated using two-sided Wilcoxon test **g,** Comparison of fraction contribution of the six SNV substitutions between non-triple negative *BRCA2*-mutant tumors vs all non-triple negative tumors. The labels for p values are as the following: ns: $p > 0.05$, *: $p <= 0.05$, **: $p <= 0.01$, ***: $p <= 0.001$, ****: $p <= 0.0001$. **h-i,** Comparison of fraction contribution of COSMIC signature 3 (**h**) and distribution of microhomology mediated deletion (**i**) between *BRCA1*-mutated triple negative tumors or non-triple *BRCA1*-mutated negative tumors with their histology control. P-values calculated using two-sided Wilcoxon test **j-k,** Copy number plots for biallelic mutated *BRCA1*(**j**) and *BRCA2* (**k**) tumors from TCGA breast cancer cohort. (**L).** Comparison of fraction copy number altered genome (FCNA) between *BRCA1* and *BRCA2*-mutant tumors and histology-matched control tumors. Data show significantly higher FCNA in *BRCA1*-mutant tumors relative to histology-matched controls, while no such effect was observed for *BRCA2*-mutant tumors. P-values calculated using two-sided Wilcoxon test.

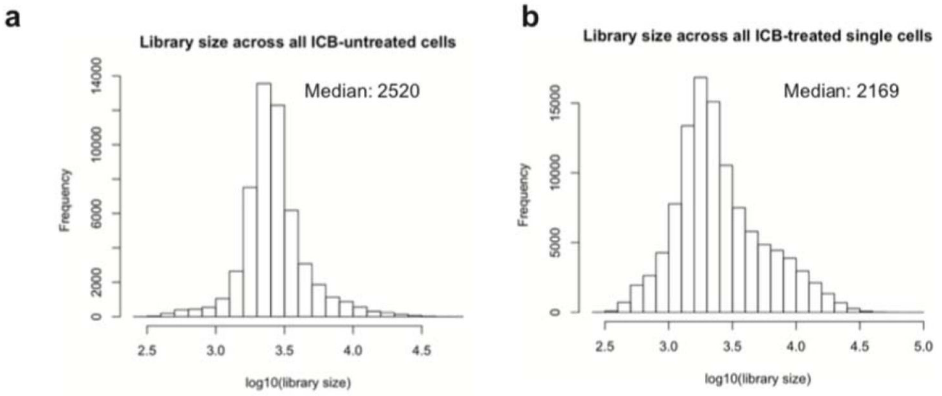

c

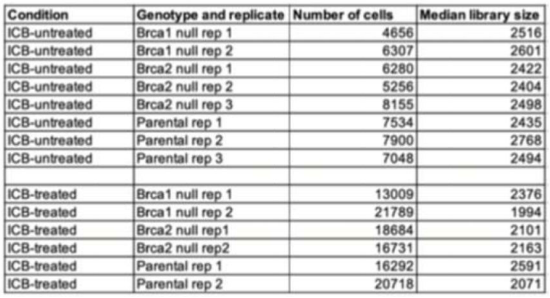

Condition	Genotype and replicate	Number of cells	Median library size
ICB-untreated	Brca1 null rep 1	4656	2516
ICB-untreated	Brca1 null rep 2	6307	2601
ICB-untreated	Brca2 null rep 1	6280	2422
ICB-untreated	Brca2 null rep 2	5256	2404
ICB-untreated	Brca2 null rep 3	8155	2498
ICB-untreated	Parental rep 1	7534	2435
ICB-untreated	Parental rep 2	7900	2768
ICB-untreated	Parental rep 3	7048	2494
ICB-treated	Brca1 null rep 1	13009	2376
ICB-treated	Brca1 null rep 2	21789	1994
ICB-treated	Brca2 null rep1	18684	2101
ICB-treated	Brca2 null rep2	16731	2163
ICB-treated	Parental rep 1	16292	2591
ICB-treated	Parental rep 2	20718	2071

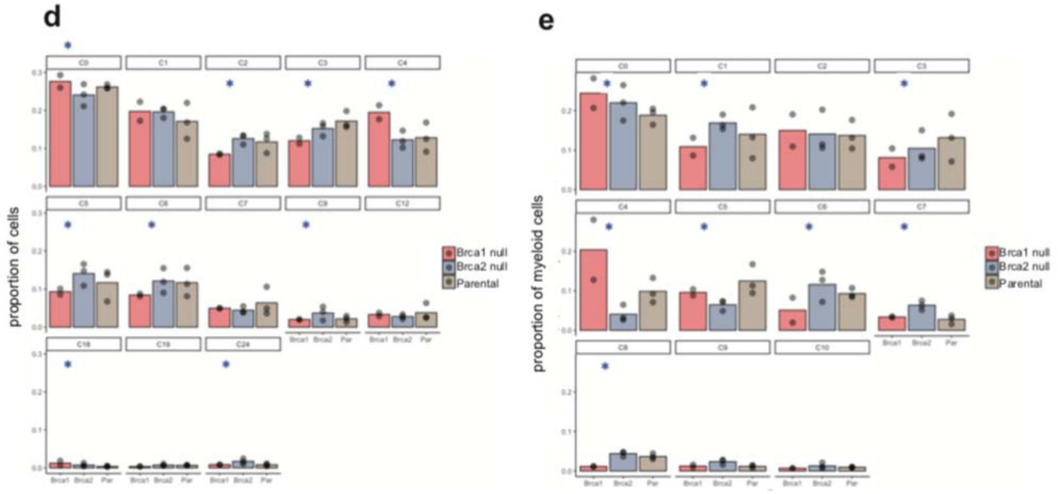

Extended Data Fig. 8 |. Single cell library sizes, replicates, and proportions of clusters across ICB-untreated Brca2^{null} and Brca1^{null} tumors and parental tumors.

a, Library size distribution for ICB-untreated single cells **b**, Library size distribution for ICB-treated single cells. **c**, Number of cells for each replicate used in scRNA-seq analyses. **d**, Proportion of all cells attributed to each T cell cluster from Fig 5 (ICB-untreated mice) from Brca2^{null}, Brca1^{null}, and parental tumors. **e,** Proportion of all myeloid cells attributed to each myeloid cell cluster from Fig 5 (ICB-untreated mice) from Brca2^{null}, Brca1^{null}, and parental tumors. Stars represent FDR p-value < 0.05 from two-sided Fisher's exact test comparing cluster proportions in Brca2^{null} and Brca1^{null} mice.

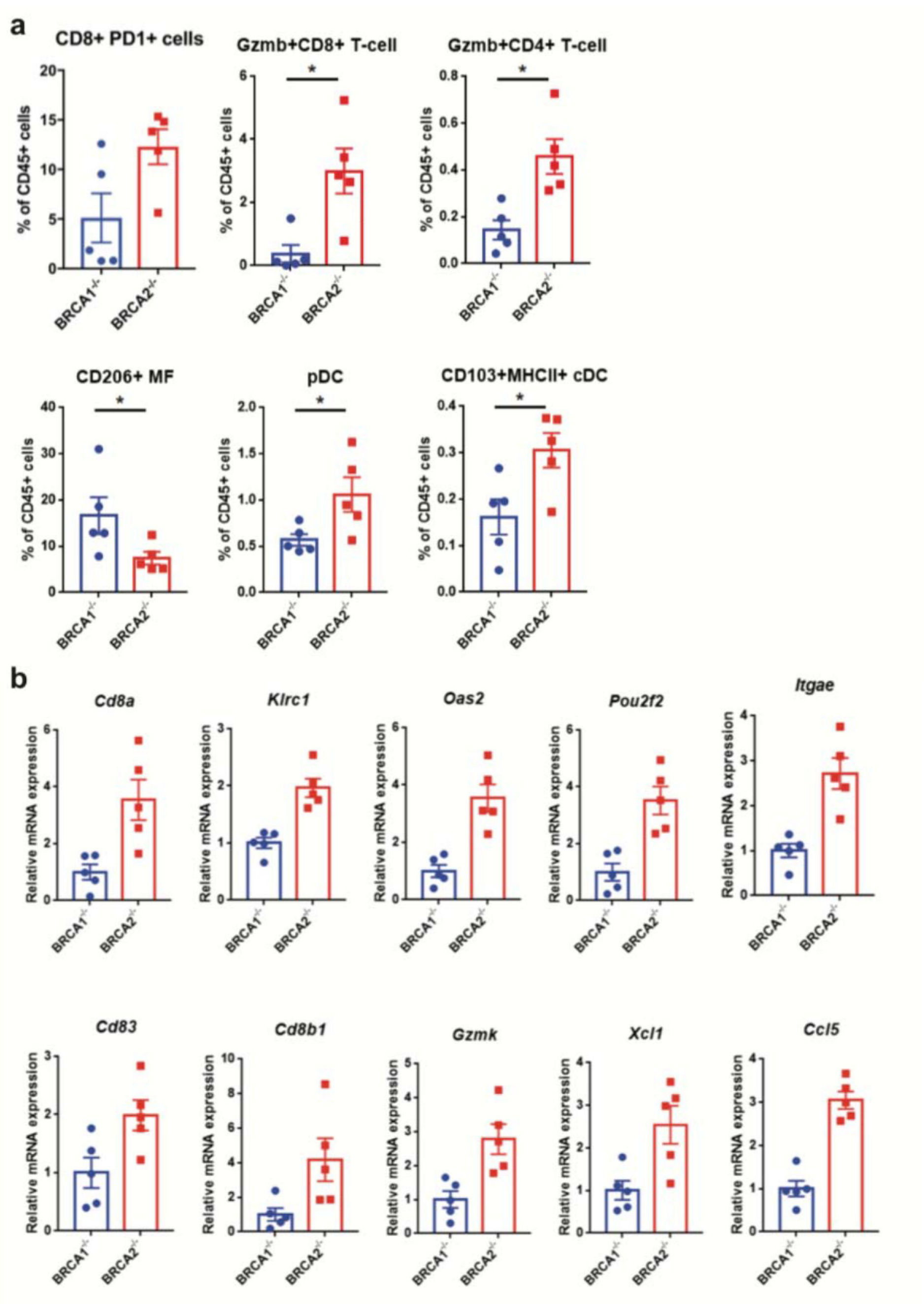

Extended Data Fig. 9 |. Experimental validation of sc-RNA-seq and bulk RNA-seq results on untreated 4T1 Brca1$^{\text{null}}$ and Brca2$^{\text{null}}$ tumors.

a. Flow cytometry validation of several key immune cell populations including the Gmzb+ activated Cd8+ and Cd4+ T cells, CD206+ suppressive TAM, pDC and Cd103+ conventional DC, n=5 independent biological replicates. **b.** QRT-PCR validation of the most upregulated inflammation related genes in Brca1$^{\text{null}}$ vs Brca2$^{\text{null}}$ tumors, n=5 independent biological replicates. Data are presented as mean values +/− SEM.

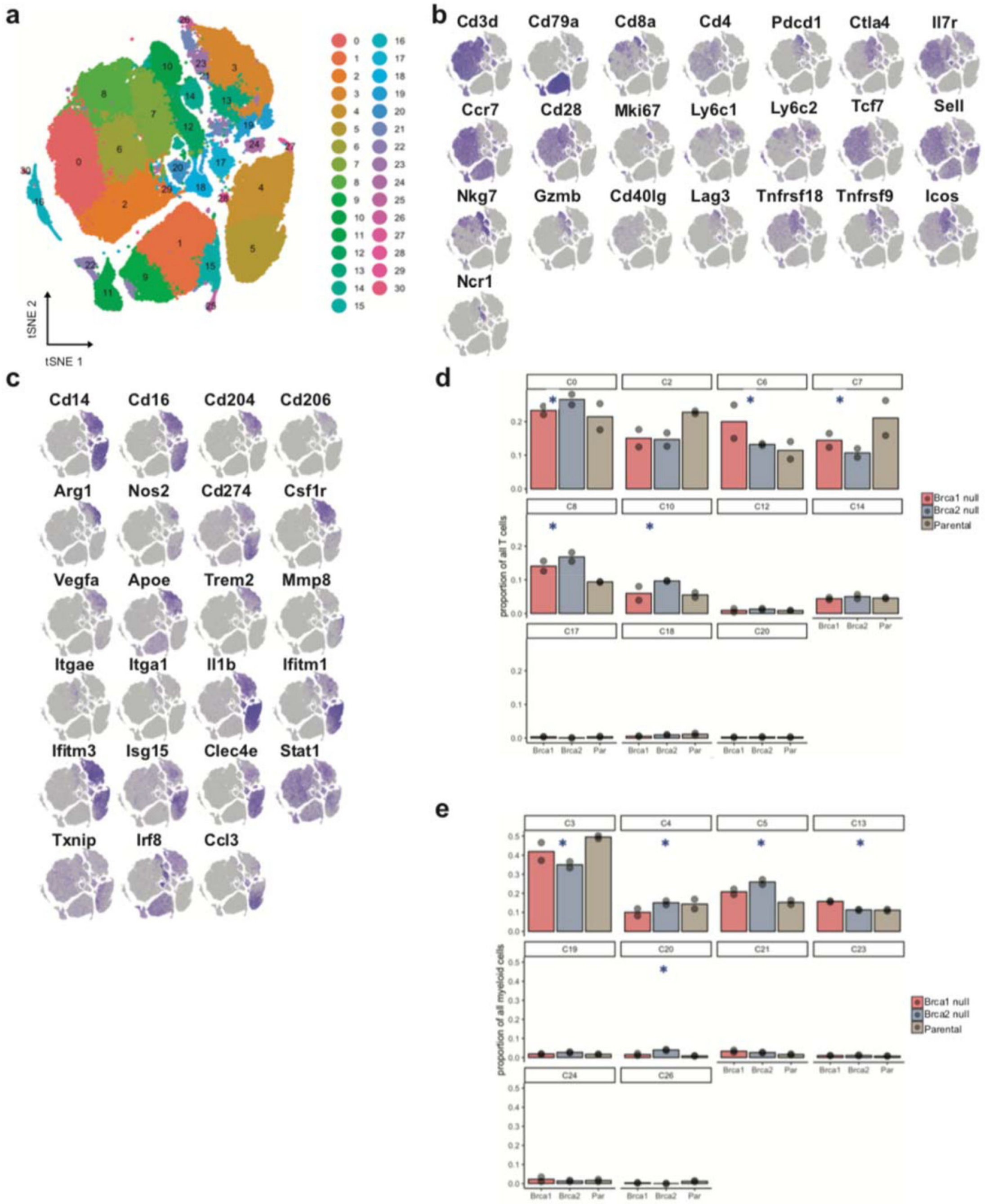

Extended Data Fig. 10 |. Single cell RNA-seq analysis reveals marked heterogeneity within 4T1 murine tumors and enrichment of distinct T cell populations in post anti-PD1 antibody therapy Brca1^{null} and Brca2^{null} tumors.

a, t-SNE plot after dimensionality reduction and Phenograph clustering yields 31 distinct clusters afrom post-treated Brca1^{null} and Brca2^{null} tumors as well as parental tumor. **b**, t-SNE plots from **a** overlaid with log-normalized expression of select markers spanning T cell and NK cell clusters. **c**, t-SNE plots from a overlaid with log-normalized expression of select markers spanning myeloid cell clusters. **d**, Proportion of all cells attributed to each T cell cluster from a (ICB-untreated mice) from Brca1^{null}, Brca2^{null} and parental tumors, for clusters with more than 100 cells. **e**, Proportion of all cells attributed to each T cell cluster from a (ICB-untreated mice) from Brca1^{null}, Brca2^{null}, and parental tumors, for clusters with more than 100 cells. Stars represent FDR $P < 0.05$ from two-sided Fisher's exact test comparing cluster proportions in Brca2^{nul}l mice and Brca1^{null} mice.

Supplementary Material

Refer to Web version on PubMed Central for supplementary material.

ACKNOWLEDGEMENTS

We thank the members of the Chan lab, the Immunogenomics and Precision Oncology Platform, the Marie-Josée and Henry R. Kravis Center for Molecular Oncology, the Medical Genetics Service at MSKCC, and the Dept. of Pathology for helpful discussions. We also thank MSKCC core laboratories including the Anti-Tumor Assessment, Molecular Cytology, Cytogenetics, and Flow Cytometry cores. JSR-F and SNP are funded in part by the Breast Cancer Research Foundation. This study was funded in part through the NIH/NCI Cancer Center Support Grant P30 CA008748. We acknowledge funding sources including Pershing Square Sohn Cancer Research grant (TAC), the PaineWebber Chair (TAC), Stand Up 2 Cancer (TAC), NIH R01 CA205426, NIH R35 CA232097 (TAC), the STARR Cancer Consortium (TAC), AACR Translational Immunology (RMS), NIH Director's Early Independence Award, DP5-OD028171 (RMS), Burroughs Wellcome Fund Career Award for Medical Scientists (RMS), Precision Immunotherapy Kidney Cancer Fund (TAC, RJM), Frederick Adler Fund (LGTM), and NIH U54 OD020355 (EDS).

COMPETING INTERESTS

TAC is a co-founder of Gritstone Oncology and holds equity. TAC holds equity in An2H. TAC acknowledges grant funding from Bristol-Myers Squibb, AstraZeneca, Illumina, Pfizer, An2H, and Eisai. LGTM receives research funding from AstraZeneca. TAC has served as an advisor for Bristol-Myers Squibb, Illumina, Eisai, and An2H. MSK has licensed the use of TMB for the identification of patients that benefit from immune checkpoint therapy to PGDx. MSK, RMS, LGTM and TAC receive royalties as part of this licensing agreement. JSR-F reports personal/consultancy fees from Goldman Sachs and membership of the advisory boards of VolitionRx, Page.AI, Invicro, Roche, Genentech and Ventana, outside the submitted work. NR has received research funding from BMS, Pfizer, and REPARE Therapeutics, and has served as an ad-hoc consultant to Illumina, REPARE Therapeutics, and Mirati Therapeutics.

REFERENCES

1. Hugo W et al. Genomic and Transcriptomic Features of Response to Anti-PD-1 Therapy in Metastatic Melanoma. Cell 165, 35–44 (2016). [PubMed: 26997480]
2. McGranahan N et al. Clonal neoantigens elicit T cell immunoreactivity and sensitivity to immune checkpoint blockade. Science 351, 1463–1469 (2016). [PubMed: 26940869]
3. Rizvi NA et al. Cancer immunology. Mutational landscape determines sensitivity to PD-1 blockade in non-small cell lung cancer. Science 348, 124–128 (2015). [PubMed: 25765070]
4. Snyder A et al. Genetic Basis for Clinical Response to CTLA-4 Blockade in Melanoma. 371, 2189–2199 (2014).
5. Mouw KW, Goldberg MS, Konstantinopoulos PA & D'Andrea AD DNA Damage and Repair Biomarkers of Immunotherapy Response. Cancer Discovery 7, 675–693 (2017). [PubMed: 28630051]
6. Le DT et al. Mismatch repair deficiency predicts response of solid tumors to PD-1 blockade. Science 357, 409–413 (2017). [PubMed: 28596308]
7. Ma J, Setton J, Lee NY, Riaz N & Powell SN The therapeutic significance of mutational signatures from DNA repair deficiency in cancer. Nature Communications 9, 3292 (2018).
8. Rebbeck TR et al. Association of Type and Location of BRCA1and BRCA2Mutations With Risk of Breast and Ovarian Cancer. JAMA 313, 1347–15 (2015). [PubMed: 25849179]
9. Teo MY et al. Alterations in DNA Damage Response and Repair Genes as Potential Marker of Clinical Benefit From PD-1/PD-L1 Blockade in Advanced Urothelial Cancers. J. Clin. Oncol 36, 1685–1694 (2018). [PubMed: 29489427]

10. Karzai F et al. Activity of durvalumab plus olaparib in metastatic castration-resistant prostate cancer in men with and without DNA damage repair mutations. Journal for ImmunoTherapy of Cancer 6, 141 (2018). [PubMed: 30514390]
11. Azizi E et al. Single-Cell Map of Diverse Immune Phenotypes in the Breast Tumor Microenvironment. Cell 174, 1293–1308.e36 (2018). [PubMed: 29961579]
12. Zhang AW et al. Interfaces of Malignant and Immunologic Clonal Dynamics in Ovarian Cancer. Cell 173, 1755–1769.e22 (2018). [PubMed: 29754820]
13. Nanda R et al. Pembrolizumab in Patients With Advanced Triple-Negative Breast Cancer: Phase Ib KEYNOTE-012 Study. J. Clin. Oncol 34, 2460–2467 (2016). [PubMed: 27138582]
14. Disis ML et al. Efficacy and Safety of Avelumab for Patients With Recurrent or Refractory Ovarian Cancer: Phase 1b Results From the JAVELIN Solid Tumor Trial. JAMA Oncol 5, 393 (2019). [PubMed: 30676622]
15. Zehir A et al. Mutational landscape of metastatic cancer revealed from prospective clinical sequencing of 10,000 patients. Nat Med 23, 703–713 (2017). [PubMed: 28481359]
16. Samstein RM et al. Tumor mutational load predicts survival after immunotherapy across multiple cancer types. Nat Genet 51, 202–206 (2019). [PubMed: 30643254]
17. Prakash R, Zhang Y, Feng W & Jasin M Homologous recombination and human health: the roles of BRCA1, BRCA2, and associated proteins. Cold Spring Harb Perspect Biol 7, a016600 (2015). [PubMed: 25833843]
18. Powell SN & Kachnic LA Roles of BRCA1 and BRCA2 in homologous recombination, DNA replication fidelity and the cellular response to ionizing radiation. Oncogene 22, 5784–5791 (2003). [PubMed: 12947386]
19. Koh G, Zou X & Nik-Zainal S Mutational signatures: experimental design and analytical framework. Genome Biol. 21, 37–13 (2020). [PubMed: 32059681]
20. Davies H et al. HRDetect is a predictor of BRCA1 and BRCA2 deficiency based on mutational signatures. Nat Med 23, 517–525 (2017). [PubMed: 28288110]
21. Francis JC et al. Whole-exome DNA sequence analysis of Brca2- and Trp53-deficient mouse mammary gland tumours. J. Pathol. 236, 186–200 (2015). [PubMed: 25692405]
22. Chockley PJ & Keshamouni VG Immunological Consequences of Epithelial-Mesenchymal Transition in Tumor Progression. 197, 691–698 (2016).
23. Datar I & Schalper KA Epithelial-Mesenchymal Transition and Immune Evasion during Lung Cancer Progression: The Chicken or the Egg? Clinical Cancer Research 22, 3422–3424 (2016). [PubMed: 27076625]
24. Lakhani SR et al. Multifactorial analysis of differences between sporadic breast cancers and cancers involving BRCA1 and BRCA2 mutations. JNCI Journal of the National Cancer Institute 90, 1138–1145 (1998). [PubMed: 9701363]
25. Lakhani SR et al. Prediction of BRCA1 status in patients with breast cancer using estrogen receptor and basal phenotype. Clinical Cancer Research 11, 5175–5180 (2005). [PubMed: 16033833]
26. Nolan E et al. Combined immune checkpoint blockade as a therapeutic strategy for BRCA1-mutated breast cancer. Sci Transl Med 9, eaal4922 (2017). [PubMed: 28592566]
27. Liu H et al. ADORA1 Inhibition Promotes Tumor Immune Evasion by Regulating the ATF3-PD-L1 Axis. *Cancer Cell* 37, 324–339.e8 (2020). [PubMed: 32183950]
28. Moral JA et al. ILC2s amplify PD-1 blockade by activating tissue-specific cancer immunity. Nature 579, 130–135 (2020). [PubMed: 32076273]
29. Naskar D et al. Wnt5a-Rac1-NF-κB homeostatic circuitry sustains innate immune functions in macrophages. 192, 4386–4397 (2014).
30. Danaher P et al. Pan-cancer adaptive immune resistance as defined by the Tumor Inflammation Signature (TIS): results from The Cancer Genome Atlas (TCGA). 1–17 (2018). doi:10.1186/s40425-018-0367-1
31. Pereira B et al. The somatic mutation profiles of 2,433 breast cancers refines their genomic and transcriptomic landscapes. Nature Communications 7, 1–15 (2016).

32. Schaaf MB, Garg AD & Agostinis P Defining the role of the tumor vasculature in antitumor immunity and immunotherapy. Cell Death and Disease 1–14 (2018). doi:10.1038/s41419-017-0061-0
33. Wellenstein MD & de Visser KE Cancer-Cell-Intrinsic Mechanisms Shaping the Tumor Immune Landscape. Immunity 48, 399–416 (2018). [PubMed: 29562192]
34. Riaz N et al. Tumor and Microenvironment Evolution during Immunotherapy with Nivolumab. Cell 171, 934–949.e16 (2017). [PubMed: 29033130]
35. Benci JL et al. Tumor Interferon Signaling Regulates a Multigenic Resistance Program to Immune Checkpoint Blockade. Cell 167, 1540–1554.e12 (2016). [PubMed: 27912061]
36. Buckley NE et al. BRCA1 regulates IFN-gamma signaling through a mechanism involving the type I IFNs. Mol. Cancer Res. 5, 261–270 (2007). [PubMed: 17374731]
37. Riaz N et al. Pan-cancer analysis of bi-allelic alterations in homologous recombination DNA repair genes. Nature Communications 1–7 (2017). doi:10.1038/s41467-017-00921-w
38. Ciriello G et al. Comprehensive Molecular Portraits of Invasive Lobular Breast Cancer. Cell 163, 506–519 (2015). [PubMed: 26451490]
39. Nik-Zainal S et al. Landscape of somatic mutations in 560 breast cancer whole-genome sequences. Nature 534, 47–54 (2016). [PubMed: 27135926]
40. Timms KM et al. Association of BRCA1/2defects with genomic scores predictive of DNA damage repair deficiency among breast cancer subtypes. Breast Cancer Res 16, 123–9 (2014).
41. Davoli T, Uno H, Wooten EC & Elledge SJ Tumor aneuploidy correlates with markers of immune evasion and with reduced response to immunotherapy. Science 355, eaaf8399–16 (2017). [PubMed: 28104840]
42. Karn T et al. Association Between Genomic Metrics and Immune Infiltration in Triple-Negative Breast Cancer. JAMA Oncol 3, 1707–1711 (2017). [PubMed: 28750120]
43. Levine JH et al. Data-Driven Phenotypic Dissection of AML Reveals Progenitor-like Cells that Correlate with Prognosis. Cell 162, 184–197 (2015). [PubMed: 26095251]
44. Lange SM et al. l-Citrulline Metabolism in Mice Augments CD4+ T Cell Proliferation and Cytokine Production In Vitro, and Accumulation in the Mycobacteria-Infected Lung. Front Immunol 8, 1561 (2017). [PubMed: 29201027]
45. Sade-Feldman M et al. Defining T Cell States Associated with Response to Checkpoint Immunotherapy in Melanoma. Cell 176, 404 (2019). [PubMed: 30633907]
46. Wagner J et al. A Single-Cell Atlas of the Tumor and Immune Ecosystem of Human Breast Cancer. Cell 177, 1330–1345.e18 (2019). [PubMed: 30982598]
47. Gubin MM et al. High-Dimensional Analysis Delineates Myeloid and Lymphoid Compartment Remodeling during Successful Immune-Checkpoint Cancer Therapy. Cell 175, 1443 (2018). [PubMed: 30445041]
48. Strickland KC et al. Association and prognostic significance of BRCA1/2-mutation status with neoantigen load, number of tumor-infiltrating lymphocytes and expression of PD-1/PD-L1 in high grade serous ovarian cancer. Oncotarget 7, 13587–13598 (2016). [PubMed: 26871470]
49. Kraya AA et al. Genomic Signatures Predict the Immunogenicity of BRCA-Deficient Breast Cancer. Clinical Cancer Research (2019). doi:10.1158/1078-0432.CCR-18-0468
50. Smid M et al. Breast cancer genome and transcriptome integration implicates specific mutational signatures with immune cell infiltration. Nature Communications 7, 1–9 (2016).
51. Ovarian Tumor Tissue Analysis (OTTA) Consortium et al. Dose-Response Association of CD8 +Tumor-Infiltrating Lymphocytes and Survival Time in High-Grade Serous Ovarian Cancer. JAMA Oncol 3, e173290–9 (2017). [PubMed: 29049607]
52. Andrews HN et al. BRCA1 regulates the interferon gamma-mediated apoptotic response. J Biol Chem 277, 26225–26232 (2002). [PubMed: 12011077]
53. Dirix LY et al. Avelumab, an anti-PD-L1 antibody, in patients with locally advanced or metastatic breast cancer: a phase 1b JAVELIN Solid Tumor study. Breast Cancer Res Treat 167, 671–686 (2017). [PubMed: 29063313]

54. Emens LA et al. Long-term Clinical Outcomes and Biomarker Analyses of Atezolizumab Therapy for Patients With Metastatic Triple-Negative Breast Cancer: A Phase 1 Study. JAMA Oncol 5, 74–82 (2019). [PubMed: 30242306]
55. Chabanon RM et al. PARP inhibition enhances tumor cell-intrinsic immunity in ERCC1-deficient non-small cell lung cancer. J Clin Invest 129, 1211–1228 (2019). [PubMed: 30589644]
56. Pantelidou C et al. PARP Inhibitor Efficacy Depends on CD8+ T-cell Recruitment via Intratumoral STING Pathway Activation in BRCA-Deficient Models of Triple-Negative Breast Cancer. Cancer Discovery 9, 722–737 (2019). [PubMed: 31015319]
57. Reisländer T et al. BRCA2 abrogation triggers innate immune responses potentiated by treatment with PARP inhibitors. Nature Communications 10, 3143–13 (2019).
58. Heijink AM et al. BRCA2 deficiency instigates cGAS-mediated inflammatory signaling and confers sensitivity to tumor necrosis factor-alpha-mediated cytotoxicity. Nature Communications 10, 100 (2019).
59. Domchek SM et al. Abstract PD6–11: An open-label, multitumor, phase II basket study of olaparib and durvalumab (MEDIOLA): Results in germline BRCA-mutated (gBRCAm) HER2-negative metastatic breast cancer (MBC). Cancer Research 78, PD6–11–PD6–11 (2018).
60. Matsuo K et al. Nivolumab use for BRCA gene mutation carriers with recurrent epithelial ovarian cancer: A case series. Gynecol Oncol Rep 25, 98–101 (2018). [PubMed: 29998185]
61. Cheng DT et al. Memorial Sloan Kettering-Integrated Mutation Profiling of Actionable Cancer Targets (MSK-IMPACT) A Hybridization Capture-Based Next-Generation Sequencing Clinical Assay for Solid Tumor Molecular Oncology. The Journal of Molecular Diagnostics 17, 251–264 (2015). [PubMed: 25801821]
62. Cerami E et al. The cBio cancer genomics portal: an open platform for exploring multidimensional cancer genomics data. Cancer Discovery 2, 401–404 (2012). [PubMed: 22588877]
63. Cibulskis K et al. Sensitive detection of somatic point mutations in impure and heterogeneous cancer samples. Nature Biotechnology 31, 213–219 (2013).
64. Mandal R et al. Genetic diversity of tumors with mismatch repair deficiency influences anti-PD-1 immunotherapy response. Science 364, 485–491 (2019). [PubMed: 31048490]
65. Poplin R et al. A universal SNP and small-indel variant caller using deep neural networks. Nature Biotechnology 36, 983–987 (2018).
66. Cingolani P et al. A program for annotating and predicting the effects of single nucleotide polymorphisms, SnpEff: SNPs in the genome of Drosophila melanogaster strain w1118; iso-2; iso-3. Fly (Austin) 6, 80–92 (2012). [PubMed: 22728672]
67. Joung J et al. Genome-scale CRISPR-Cas9 knockout and transcriptional activation screening. Nature Protocols 12, 828–863 (2017). [PubMed: 28333914]
68. Blokzijl F, Janssen R, van Boxtel R & Cuppen E MutationalPatterns: comprehensive genome-wide analysis of mutational processes. Genome Medicine 10, 33 (2018). [PubMed: 29695279]
69. Love MI, Huber W & Anders S Moderated estimation of fold change and dispersion for RNA-seq data with DESeq2. Genome Biol. 15, 31–21 (2014).
70. Leek JT, Taub MA & Rasgon JL A statistical approach to selecting and confirming validation targets in -omics experiments. BMC Bioinformatics 13, 150 (2012). [PubMed: 22738145]
71. Senbabaoglu Y et al. Tumor immune microenvironment characterization in clear cell renal cell carcinoma identifies prognostic and immunotherapeutically relevant messenger RNA signatures. Genome Biol. 1–25 (2016). doi:10.1186/s13059-016-1092-z [PubMed: 26753840]
72. Anderson MJ Permutational Multivariate Analysis of Variance (PERMANOVA). 18, 1–15 (John Wiley & Sons, Ltd, 2014).
73. Anderson MJ & Santana-Garcon J Measures of precision for dissimilarity-based multivariate analysis of ecological communities. Ecol. Lett 18, 66–73 (2015). [PubMed: 25438826]
74. Butler A, Hoffman P, Smibert P, Papalexi E & Satija R Integrating single-cell transcriptomic data across different conditions, technologies, and species. Nature Biotechnology 36, 411–420 (2018).
75. Stuart T et al. Comprehensive Integration of Single-Cell Data. Cell 177, 1888–1902.e21 (2019). [PubMed: 31178118]

76. Lun ATL, McCarthy DJ & Marioni JC A step-by-step workflow for low-level analysis of single-cell RNA-seq data with Bioconductor. F1000Res 5, 2122 (2016). [PubMed: 27909575]

77. Maaten L & hinton G Visualizing Data using t-SNE. JMLR 9, 2579–2605 (2008).

78. Shen R & Seshan VE FACETS: allele-specific copy number and clonal heterogeneity analysis tool for high-throughput DNA sequencing. Nucleic Acids Research 44, e131–e131 (2016). [PubMed: 27270079]

79. Shukla SA et al. Comprehensive analysis of cancer-associated somatic mutations in class I HLA genes. Nat Biotechnol 33, 1152–1158 (2015). [PubMed: 26372948]

80. Hoof I et al. NetMHCpan, a method for MHC class I binding prediction beyond humans. Immunogenetics 61, 1–13 (2008). [PubMed: 19002680]

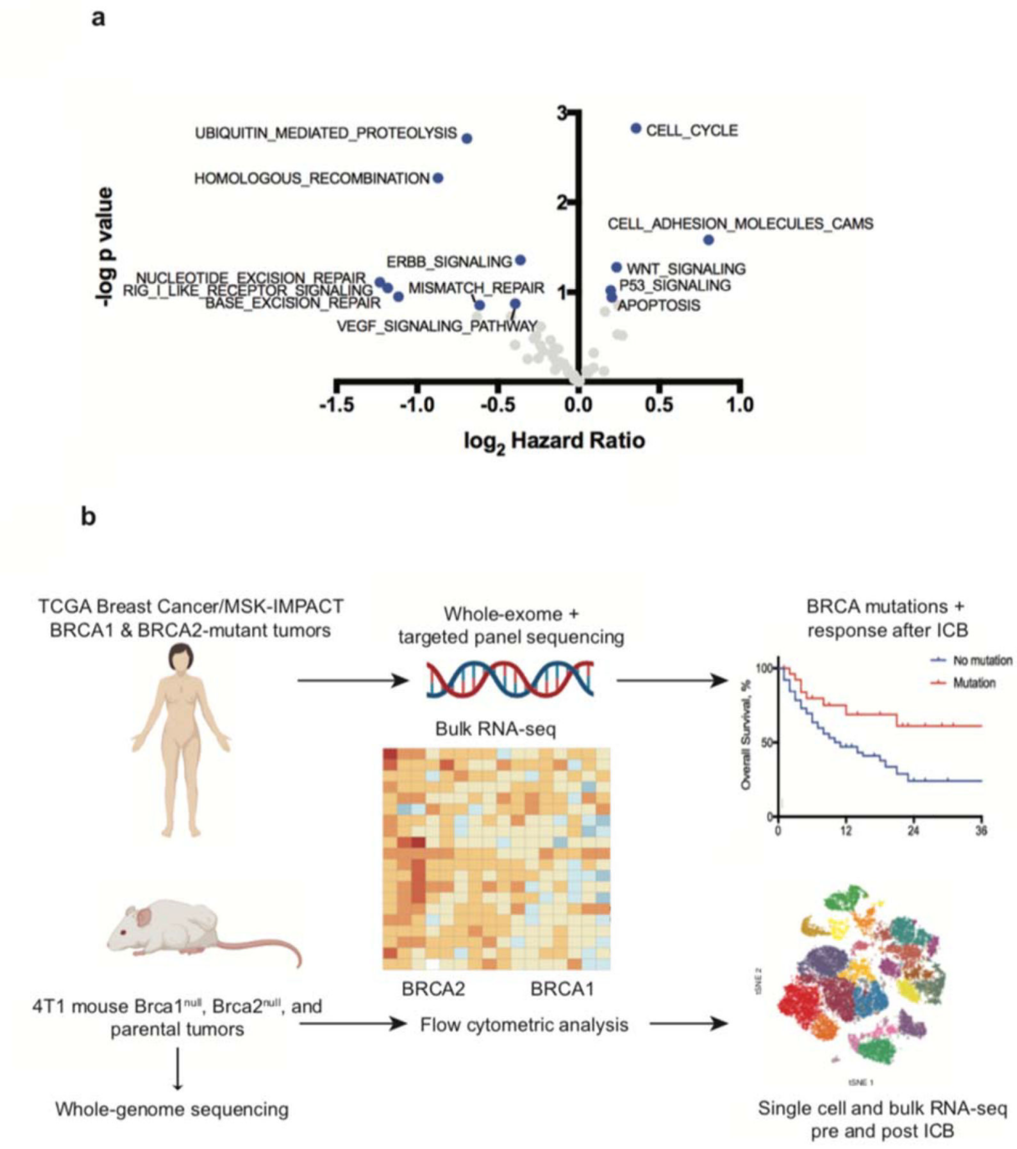

Fig 1: Immunogenomic analyses of the association of homologous recombination deficiency with response to immune checkpoint inhibitors.

a, Association of truncating somatic mutations in genes from 52 KEGG pathways sequenced by the MSK-IMPACT gene panel and improved survival after immune checkpoint inhibitor (ICB) administration. Hazard ratios and p values calculated using Cox proportional hazards model comparing survival for patients with a truncating mutation in each pathway vs. those without a mutation. Selected pathways are shown in blue. An HR pathway mutation was associated with an improved OS (hazard ratio 0.55, p = 0.005, FDR < 0.10, two-sided log-rank test). Analysis was performed on 2195 patients. Plot shows nominal unadjusted p-values. **b,** Schematic of experimental design. Whole genome, targeted panel, and bulk and single cell transcriptomic sequencing from murine and human tumors were used to analyze the effect of mutations in *BRCA1* and *BRCA2* on the tumor-immune microenvironment and response to ICB.

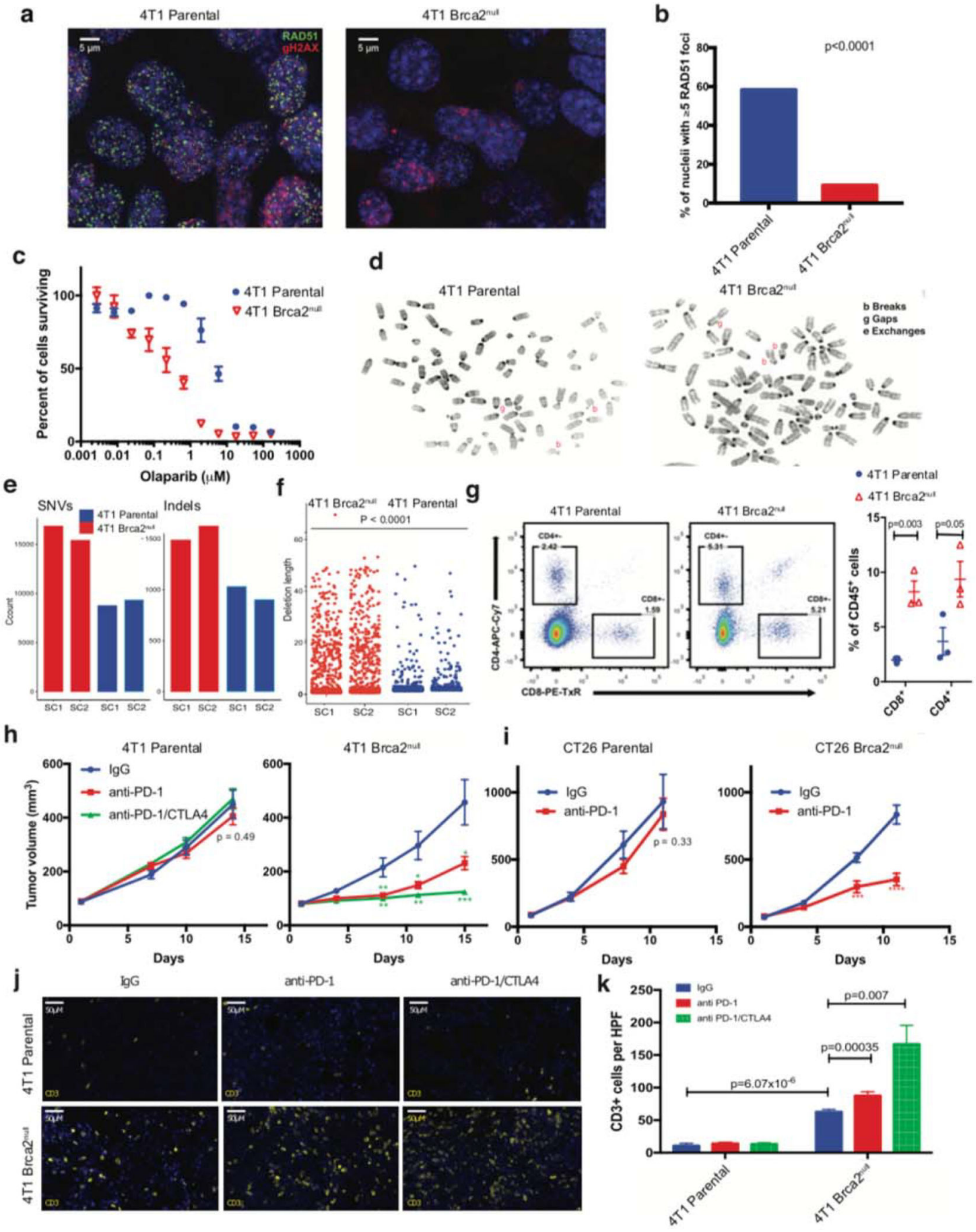

Fig 2: Enhanced response to checkpoint blockade immunotherapy in syngeneic mouse models of Brca2 deficiency.

a, Representative immunofluorescence images of parental (left) and Brca2^{null} (right) 4T1 murine breast carcinoma cells 4 hours after 10 Gy irradiation stained with DAPI and antibodies to Rad51 (green) and gamma-H2ax (red). **b,** Quantification of immunofluorescence analysis described in **a**. P value represents two-sided Fisher's exact test of the relative proportion of nuclei containing greater than 5 Rad51 foci in parental compared to Brca2^{null} cells n=173 and 109 cells analyzed, respectively **c,** *In vitro* relative viable cell count in the presence of PARP inhibitor olaparib at indicated concentrations after 96 hours in three independent assays. Data are presented as mean values +/− SEM. **d,** Representative images of parental (left) and Brca2^{null} (right) 4T1 cell karyotype analysis demonstrating increased double strand breaks. **e,** Counts of whole-genome SNVs and indels in 4T1 Brca2^{null} and two parental single cell clones after 4 months in culture. **f,** Distribution of deletion size of indels in two single cell 4T1 Brca2^{null} clones and two parental clones. Both Brca2^{null} clones (n = 1183 and 1344 deletions for SC1 and SC2 respectively) had significantly larger deletions compared to parental clone SC1 (n = 815 deletions, $p < 0.0001$ for both, two-sided Wilcoxon test), **g**, Left: Representative flow cytometry plots demonstrating percent Cd4$^+$ and Cd8a$^+$ of Cd45$^+$ tumor infiltrating lymphocytes in 4T1 parental and Brca2^{null} mammary fat pad tumors. Right: Quantification of single experiment data with n=3 animals as shown in **g**. P value represents one-sided unpaired t test. **h**, Growth curves demonstrating tumor volumes at indicated time points from start of treatment in 4T1 parental (left) and Brca2^{null} cells (right) implanted in the mammary fat pad treated with the indicated antibodies. N=15 mice per group. P values indicate two-sided t tests at respective time points (* $p<0.05$, ** $p<0.005$,*** $p<0.0005$, **** $p<0.00005$). Data are presented as mean values +/− SEM. **i,** Growth curves demonstrating tumor volumes at indicated time points from start of treatment in CT26 parental (left) and Brca2^{null} (right) flank tumors treated with the indicated antibodies. P values indicate two-sided t tests at respective time points (* $p<0.05$, ** $p<0.005$,*** $p<0.0005$, **** $p<0.00005$). Error bars represent mean ± standard error. **j** Representative immunofluorescent images stained with Cd3-Alexa647 (Yellow) and DAPI (blue) in the indicated tumors and treatment groups. **k,** Quantification right of n=5 high powered fields (HPF, 40X) from independent tumors by observer blinded to treatment group for Cd3 positive cells as well as Cd3+Cd4+ and Cd3+Cd8a+. P values represent two-sided t test. Data are presented as mean values +/− SEM.

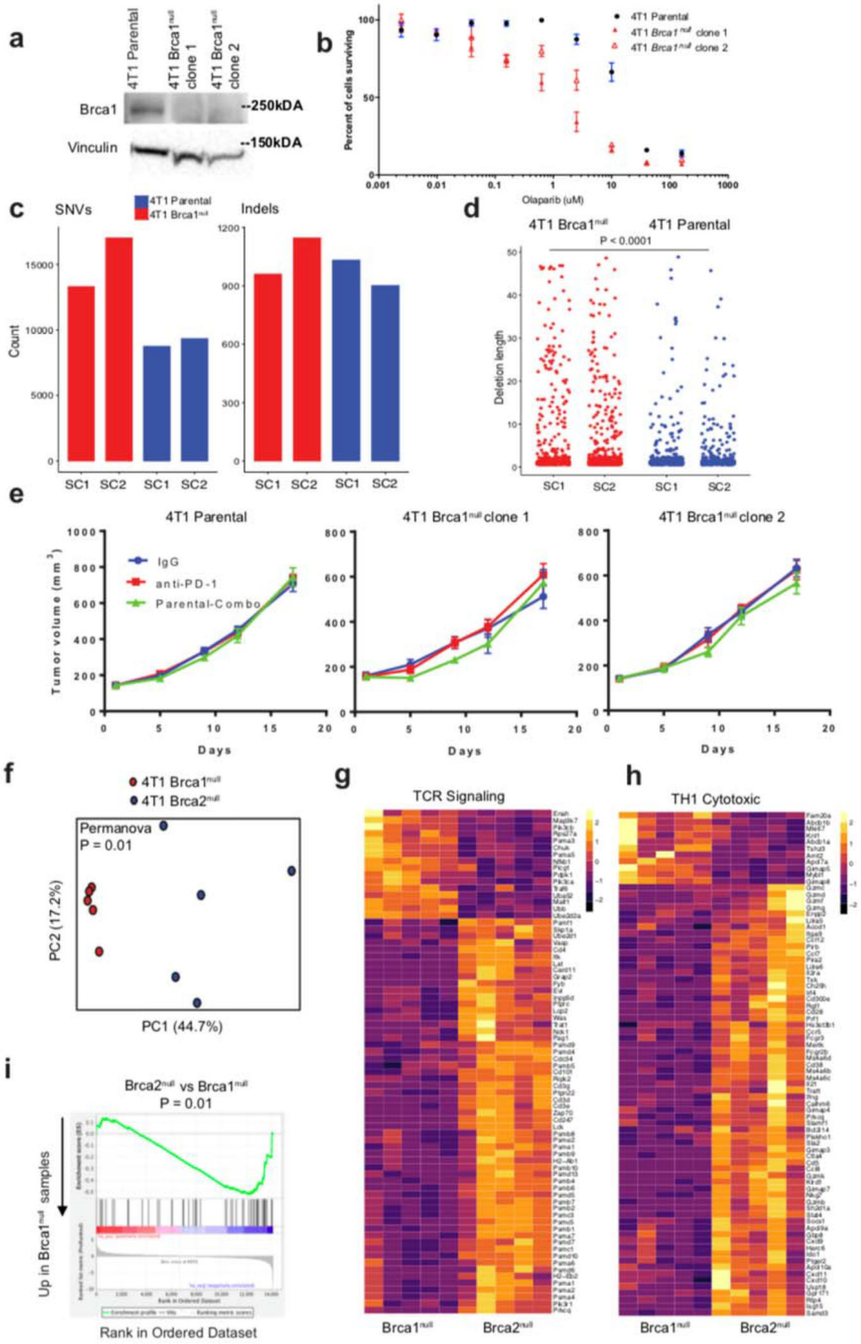

Fig 3: Differential response of *Brca1*^{null} and *Brca2*^{null} tumors to treatment with immune checkpoint inhibitors and modulation of the tumor-immune microenvironment.

a, Western blot of Brca1 in 4T1 Parental cell lines as well as two CRISPR-Cas9 edited subclones deficient in Brca1. Representative blot of 3 experiments performed with similar results. **b,** *In vitro* relative viable cell count in the presence of PARP inhibitor olaparib at indicated concentrations after 96 hours in three independent assays. **c,** Counts of SNVs and indels in two 4T1 Brca1^{null} and parental single cell clones after 4 months in culture**. d,** Distribution of deletion size of indels in two single cell 4T1 Brca1^{null} clones and two parental clones (n=4 cell lines). Both 4T1 Brca1^{null} clones (703 and 892 deletions in SC1 and SC2 respectively) have larger deletions compared to parental clone SC1 (815 deletions, $p < 0.0001$, two-sided Wilcoxon test) **e,** Growth curves demonstrating tumor volumes at indicated time points from start of treatment in 4T1 parental (left) and Brca1^{null} cells (middle and right) implanted in the mammary fat pad treated with the indicated antibodies. n = 15 mice per group. Data are presented as mean values +/− SEM. **f,** Principal component analysis of single sample gene set enrichment analysis (ssGSEA) scores for immune cells across Brca2^{null} and Brca1^{null} 4T1 mice (N = 5 biological replicates each). **g,** Heatmap of significantly differentially expressed genes from the TCR Signaling pathway from MSigDB, evaluating all differentially expressed genes (FDR $P < 0.05$, two-sided Wald test from DESeq2) between Brca2^{null} (n = 5 biological replicates) and Brca1^{null} 4T1 mice (n = 5 biological replicates). **h,** Heatmap of significantly differentially expressed genes from the Th1 Cytotoxic pathway from MSigDB, evaluating all differentially expressed genes (FDR $P < 0.05$, two-sided Wald test from DESeq2) between Brca2^{null} (n = 5 biological replicates) and Brca1^{null} (n = 5 biological replicates) 4T1 mice. **i,** GSEA enrichment plot of the immunoregulatory gene set evaluating all differentially expressed genes between 4T1 Brca2^{null} and Brca1^{null} cells in culture, indicating significant enrichment in Brca1^{null} cells. P-values calculated via two-sided GSEA pre-ranked analysis with log fold changes as input. Only one gene set (immunoregulatory gene set) was analyzed, and thus no correction for multiple testing was performed.

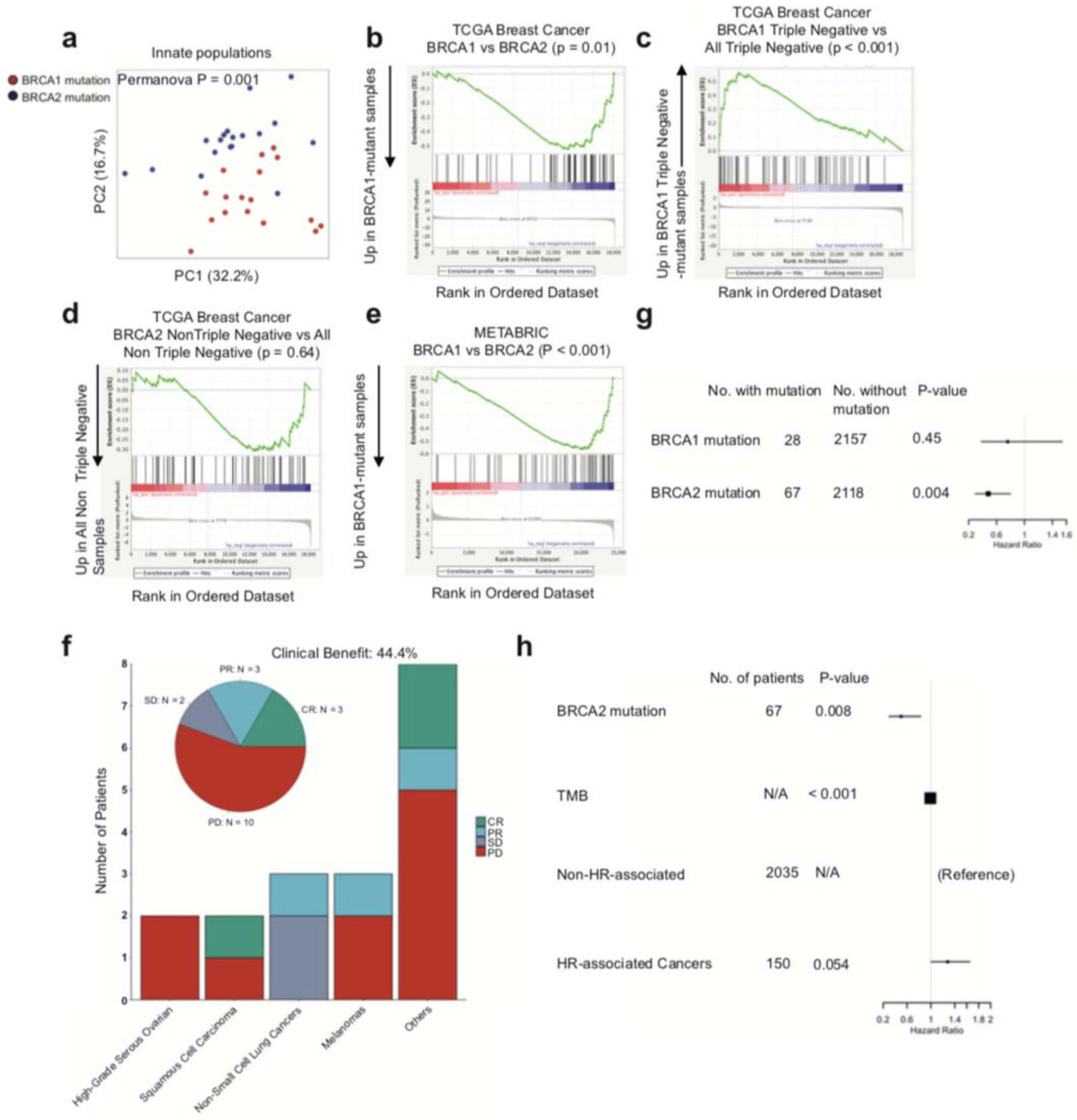

Fig 4: *BRCA1* and *BRCA2* mutations differentially modulate the tumor-immune microenvironment and response to immune checkpoint inhibitors in the TCGA breast cancer cohort and MSK-IMPACT.

a, Principal component analysis (PCA) of ssGSEA scores for innate immune cells for patients with either *BRCA1* or *BRCA2* germline or somatic biallelic mutations. P-value computed on separation between *BRCA1* mutant (n = 17) and *BRCA2* mutant (n = 18) samples using a two-sided PERMANOVA test. **b,** GSEA enrichment plot of the immunoregulatory gene set evaluating all differentially expressed genes between *BRCA2* and *BRCA1*-mutant tumors, indicating significant enrichment in *BRCA1*-mutant tumors. **c,** GSEA enrichment plot of the immunoregulatory gene set evaluating all differentially expressed genes between triple negative *BRCA1*-mutant and wild-type triple negative tumors, indicating significant enrichment in TN *BRCA1*-mutant tumors. **d,** GSEA enrichment plot of the immunoregulatory gene set evaluating all differentially expressed genes between non-triple negative *BRCA2*-mutant and wild-type non-triple negative tumors, indicating no significant enrichment. **e,** GSEA enrichment plot of the immunoregulatory gene set evaluating all differentially expressed genes between *BRCA1*-mutant and *BRCA2*-mutant tumors in the METABRIC cohort, indicating significant enrichment in *BRCA1*-mutant tumors. For **b-e**, p-values calculated via two-sided GSEA pre-ranked analysis with log fold changes as input. Only one gene set (immunoregulatory gene set) was analyzed, and thus no correction for multiple testing was performed. **f,** Proportion of patients with pathogenic identifiable *BRCA2* mutations deriving clinical benefit from ICI in MSK-IMPACT. (PR- partial response, SD- stable disease (greater than 6 months), PD-progressive disease, and CR- complete response) **g,** Overall survival of patients from anonymized MSK-IMPACT with pathogenic *BRCA2* and *BRCA1* mutations after ICB administration. P-value calculated using log-rank test. **h,** Multivariable analysis of the effect of *BRCA2* mutations on response to ICB when controlling for tumor mutation burden (TMB) and cancer type. Number of patients for TMB listed as N/A since TMB was tested as a continuous variable. P-value = 5.25e-06 for TMB. HR-associated cancers were defined as breast, prostate, pancreatic, or ovarian cancers. P-value for Non-HR-associated listed as N/A since it is the reference level. P-values are unadjusted and calculated from multivariable cox regression.

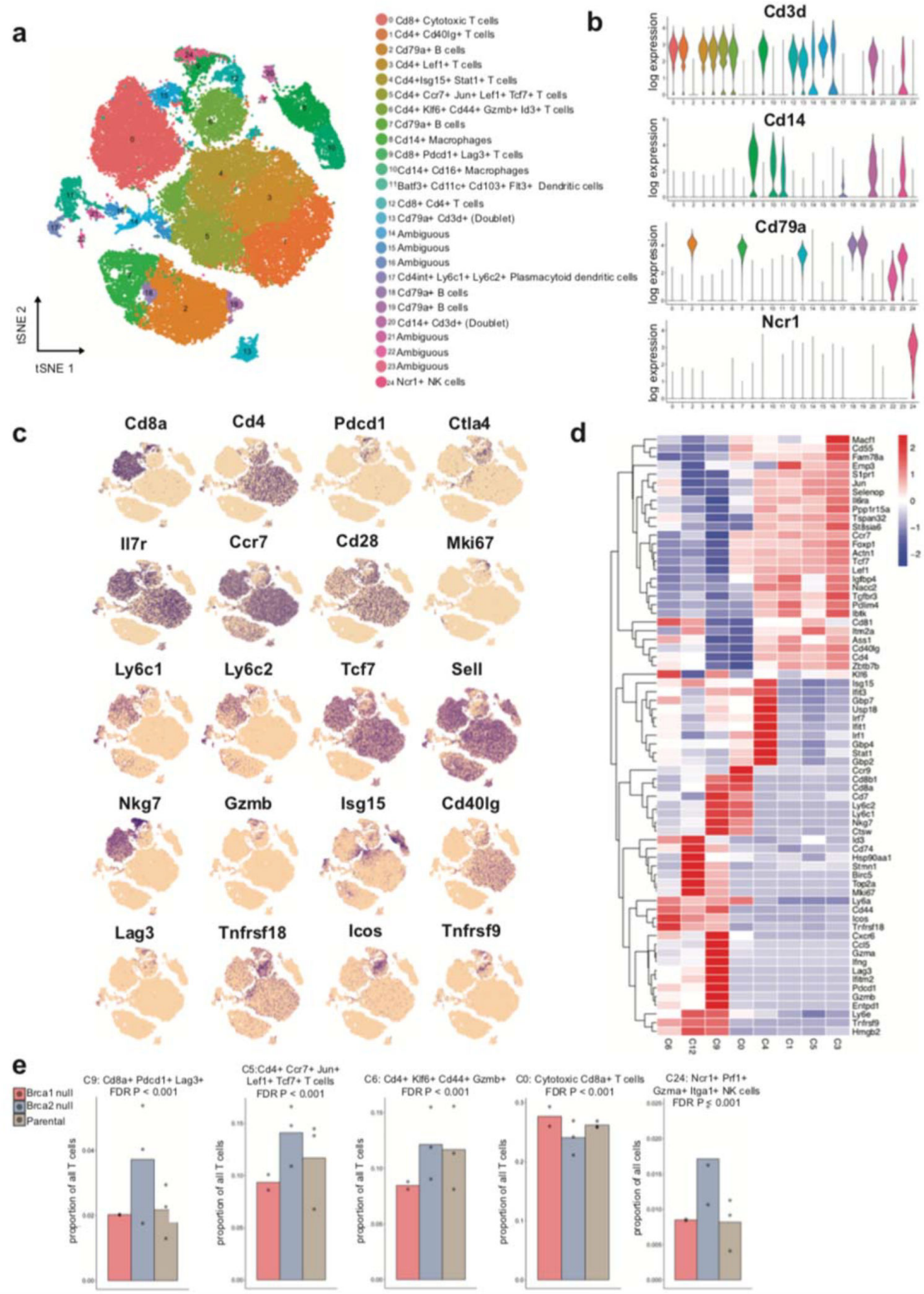

Fig 5: Single cell RNA-seq analysis reveals marked heterogeneity within 4T1 murine tumors and enrichment of distinct T cell populations in Brca1^{null} and Brca2^{null} tumors.

a, t-SNE plot after dimensionality reduction and Phenograph clustering yields 25 distinct clusters across 53136 cells from untreated Brca1^{null} and Brca2^{null} tumors as well as parental tumors. Top significantly differentially expressed genes and manual phenotype (or ambiguous, for clusters that could not be assigned a known phenotype) assignment are shown as annotations for each cluster. **b,** Violin plots showing log-normalized expression of lineage-defining immune cell markers across all clusters. Markers for T cells (*Cd3d*), myeloid cells (*Cd14*), B cells (*Cd79a*), and NK cells (*Ncr1*) are shown. **c,** t-SNE plots from **a** overlaid with log-normalized expression of select markers spanning cytotoxic, exhausted, memory, and proliferative T cell states. **d,** Heatmap of mean log-normalized expression of top differentially expressed genes per cluster, for T cell clusters. **e,** Cluster enrichments for T cell clusters and the NK cell cluster C24 in untreated tumors. Each replicate is plotted within each genotype, and barplots show mean proportion across all replicates within a genotype. n = 3 biologically independent samples for Brca2 null and Parental mice, and n = 2 biologically independent samples for Brca1 null mice. P-values calculated via two-sided Fisher's exact test comparing T cell/NK cluster proportions in Brca2 null and Brca1 null mice. C9: FDR P = 4.19e-12, C5: FDR P = 1.07e-21, C6: 6.86e-17, C0: 9.97e-10, C24: 5.81e-12. All p-values were adjusted for multiple comparisons using the Benjamini-Hochberg method.

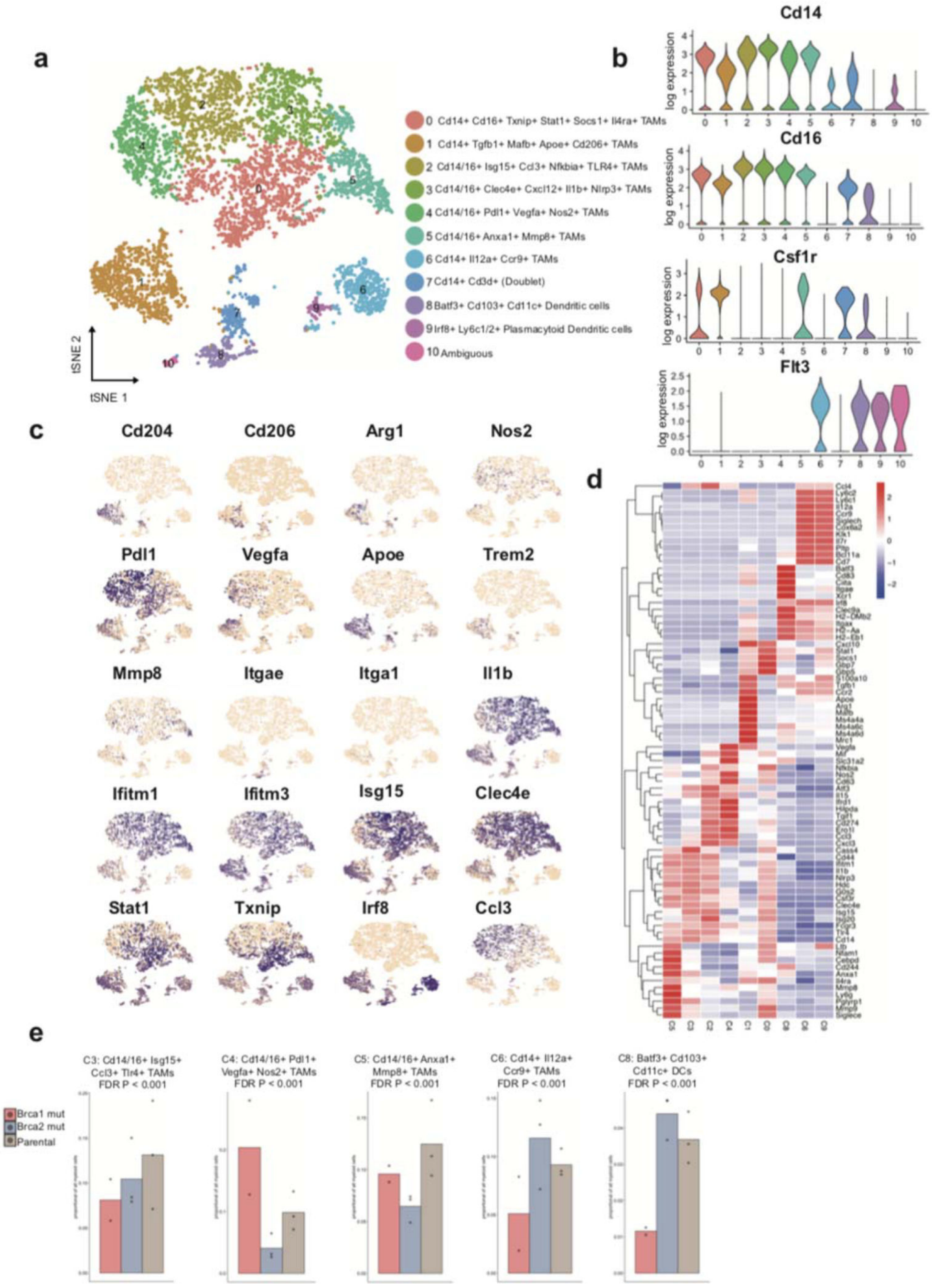

Fig 6: Single cell RNA-seq analysis reveals enrichment of distinct myeloid populations in Brca1^{null} and Brca2^{null} tumors.

a, t-SNE plot after reclustering of all *Cd3*$^{-}$ *Cd14*$^{+}$ cells from Fig. 5a after dimensionality reduction and Phenograph clustering yields 11 distinct clusters across 5390 cells from untreated Brca1 and Brca2-deficient tumors as well as parental tumors. Top significantly differentially expressed genes and manual phenotype (or ambiguous, for clusters that could not be assigned a known phenotype) assignment are shown as annotations for each cluster. **b,** Violin plots showing log-normalized expression of lineage-defining immune cell markers across all clusters. Markers for monocytes (*Cd16)*, macrophages (*Csf1r)*, and dendritic cells (*Flt3)*. **c,** t-SNE plots from **a** overlaid with log-normalized expression of select markers spanning pro- and anti-inflammatory myeloid cell states. **d,** Heatmap of mean log-normalized expression of top differentially expressed genes per cluster, for myeloid cell clusters C0-C9 **e,** Cluster enrichments (presented as fraction of all myeloid cells) in untreated tumors. Each replicate is plotted within each genotype, and barplots show mean proportion across all replicates within a genotype. n = 3 biologically independent samples for Brca2 null and Parental mice, and n = 2 biologically independent samples for Brca1 null mice. P-values calculated via two-sided Fisher's exact test comparing cluster proportions in Brca2 null and Brca1 null mice. C3: FDR P = 9.58e-05, C4: FDR P = 8.76e-47, C5: FDR P = 9.58e-05, C6: FDR P = 6.47e-05, C8: FDR P = 7.46e-07. All p-values were adjusted for multiple comparisons using the Benjamini-Hochberg method.

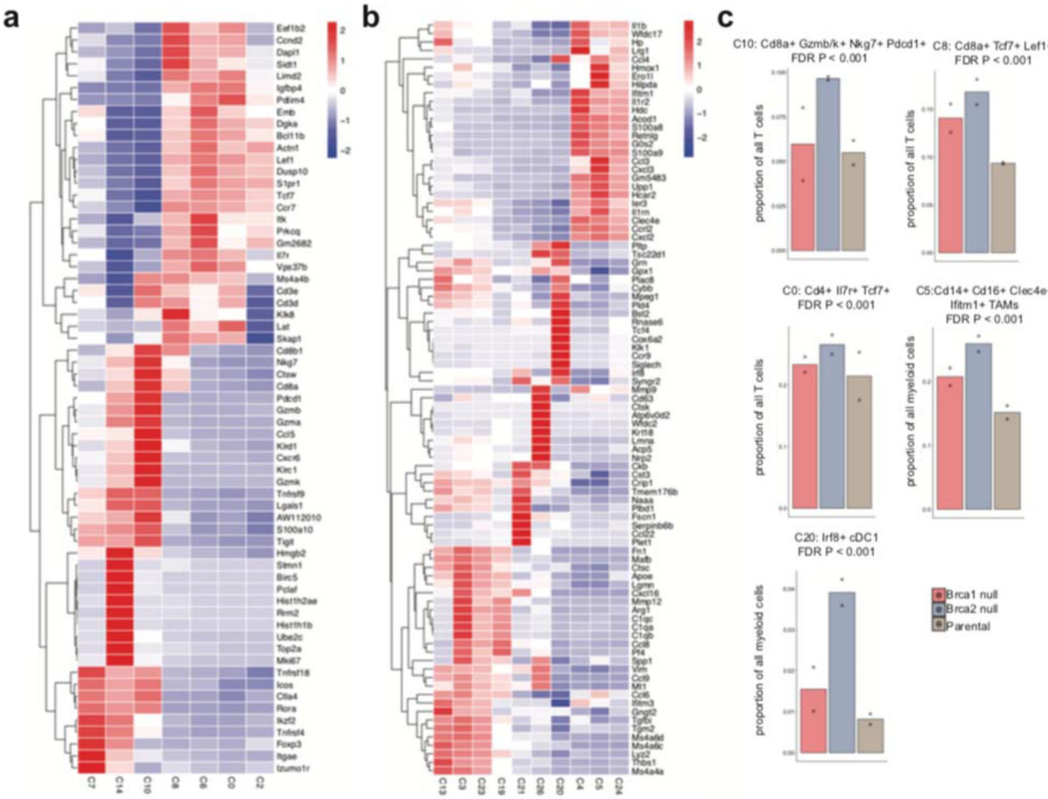

Fig 7: Single cell RNA-seq analysis reveals enrichment of distinct myeloid populations in Brca1^{null} and Brca2^{null} tumors treated with ICB.

a, Heatmap of mean log-normalized expression of top differentially expressed genes per cluster for T cell clusters **b**, Heatmap of mean log-normalized expression of top differentially expressed genes per cluster for myeloid clusters **c**, Cluster enrichments in ICB-treated tumors. Each replicate is plotted within each genotype, and barplots show mean proportion across all replicates within a genotype. n = 2 biologically independent samples for Brca1 null, Brca2 null and Parental mice, P-values calculated via two-sided Fisher's exact test comparing cluster proportions in Brca2 null and Brca1 null mice. C10: FDR P = 4.24e-25, C8: FDR P = 2.73e-13, C0: FDR P = 1.04e-11, C5: FDR P = 1.60e-05, C20: FDR P = 2.06e-06. All p-values were adjusted for multiple comparisons using the Benjamini-Hochberg method.